Effect of high-pressure heat treatment and aging on mechanical properties and very high cycle fatigue behavior of PBF-LB AlSi7Mg

Engineering Science and Technology, an International Journal 81 (2026) 102463

Contents lists available at ScienceDirect

Engineering Science and Technology, an International Journal

journal homepage: www.elsevier.com/locate/jestch

Effect of high-pressure heat treatment and aging on mechanical properties and very high cycle fatigue behavior of PBF-LB AlSi7Mg

Dinesh Shivakoti [a,1], Marta Gajewska [b,1], Mojtaba Roshan [a], MohammadBagher Mahtabi [a], Grzegorz Cios [b], Wiktor Bednarczyk [c], Donald Godfrey [d], Francisco Medina [e], Chad Beamer [f], Andrew Cassese [f], Andrea Tridello [g,i], Alessandro Benelli [h,i], Meysam Haghshenas [a,*]

[a] *Fatigue, Fracture, and Failure Laboratory (F3L), College of Engineering, University of Toledo, OH 43606, USA*
[b] *Academic Centre for Materials and Nanotechnology (ACMiN), AGH University of Kraków, Al. A. Mickiewicza 30, 30-059 Kraków, Poland*
[c] *Faculty of Metals Engineering and Industrial Computer Science, AGH University of Kraków, Al. A. Mickiewicza 30, 30-059 Kraków, Poland*
[d] *D&B Partners Consulting LLC, Phoenix, AZ 85048, USA*
[e] *Department of Aerospace and Mechanical Engineering, The University of Texas at El Paso, TX 79968, USA*
[f] *Quintus Technologies, Columbus, OH 43035, USA*
[g] *Department of Mechanical and Aerospace Engineering, Politecnico di Torino, Turin, Italy*
[h] *Department of Applied Science and Technology, Politecnico di Torino, Turin, Italy*
[i] *Inter-Departmental Multi-Disciplinary Research Centre J-TECH @PoliTO, Turin, Italy*

A R T I C L E I N F O

Keywords:
Powder bed fused-laser beam
AlSi7Mg
Very high cycle fatigue
High-pressure heat treatment
Aging

A B S T R A C T

This study investigates the influence of an innovative high-pressure heat treatment (HPHT™), a single-step process that integrates hot isostatic pressing and heat treatment, on the microstructure, mechanical response, and very-high-cycle fatigue (VHCF) behavior of powder bed fused–laser beam (PBF-LB) AlSi7Mg alloy. A comprehensive set of characterization and testing, including advanced electron microscopy, high-resolution micro-CT, uniaxial tensile testing, and ultrasonic fatigue testing, was employed to establish quantitative correlations among defect population, microstructural evolution, mechanical properties, and fatigue resistance. Fractographic analysis using optical and scanning electron microscopy enabled detailed identification of crack-initiation modes across the examined fatigue regime. The HPHT™ process produced a marked transformation of the PBF-LB microstructure, including dissolution of the characteristic Al–Si cellular network and the formation of a refined distribution of nanoscale precipitates in the aged condition. Stress amplitude–life data revealed fatigue strengths at 10^9 cycles of 479.8 MPa, 231.0 MPa, and 225.1 MPa for the as-built, HPHT™ + aged, and HPHT™ conditions, respectively. These results collectively highlight the competing roles of defect mitigation, microstructural homogenization, and precipitation hardening in governing the long-life fatigue behavior of additively manufactured AlSi7Mg, and they demonstrate the potential of HPHT™ as a process route for tailoring the balance between strength, ductility, and VHCF performance.

1. Introduction

Aluminum–silicon (Al–Si) alloys, particularly AlSi7Mg (F357) and AlSi10Mg, are among most widely printed materials through powder bed fusion–laser beam (PBF-LB) due to their desirable engineering characteristics such as low density, high specific strength, good corrosion resistance, weldability, recyclability, and relatively low cost of the powder compared to other aluminum alloys [1–3]. In PBF-LB of Al-Si

Abbreviations: BF, Bright Field; BSE, Backscattered Electrons; EBSD, Electron Backscatter Diffraction; EDS, Energy-Dispersive X-Ray Spectroscopy; FFT, Fast Fourier Transform; GP, Guinier–Preston; HAADF, High-Angle Annular Dark-Field; HCF, High-Cycle Fatigue; HIP, Hot Isostatic Pressing; HPHT™, High-Pressure Heat Treatment; HR-TEM, High-Resolution Transmission Electron Microscopy; IPF, Inverse Pole Figure; OM, Optical Microscopy; PBF-LB, Powder Bed Fusion–Laser Beam; PSD, Particle Size Distribution; SAED, Selected Area Electron Diffraction; SEM, Scanning Electron Microscopy; SLM, Selective Laser Melting; STEM, Scanning Transmission Electron Microscopy; URQ®, Uniform Rapid Quenching; USF, Ultrasonic Fatigue; VHCF, Very High Cycle Fatigue; XCT, X-Ray Computed Tomography.

* Corresponding author.
E-mail address: Meysam.haghshenas@utoledo.edu (M. Haghshenas).

[1] Equal contribution.

https://doi.org/10.1016/j.jestch.2026.102463
Received 16 April 2026; Received in revised form 31 May 2026; Accepted 6 July 2026
Available online 10 July 2026

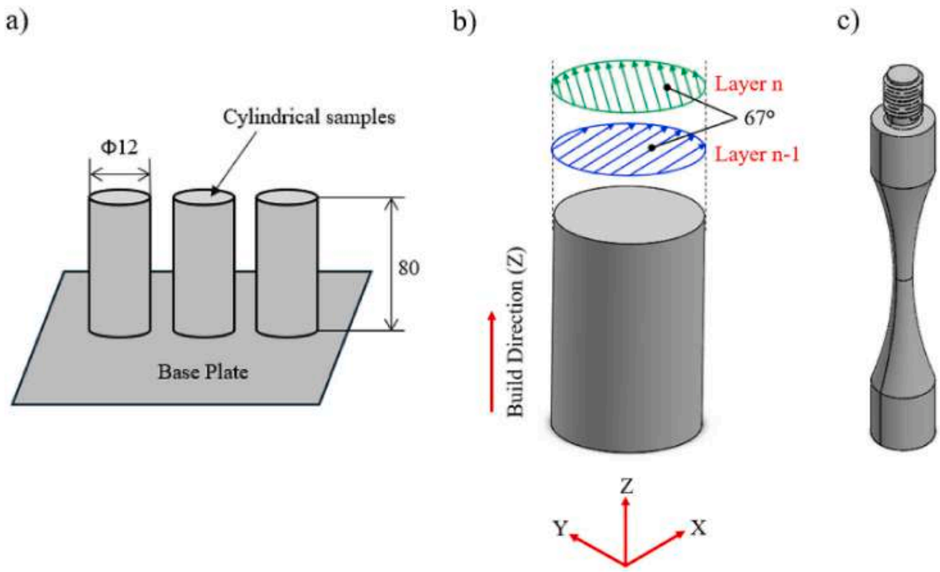

Fig. 1. (a) Fabricated cylindrical PBF-LB AlSi7Mg samples. (b) The 'layer-by-layer' scanning strategy with a rotation angle of 67° for each layer. (c) Hourglass VHCF test specimen.

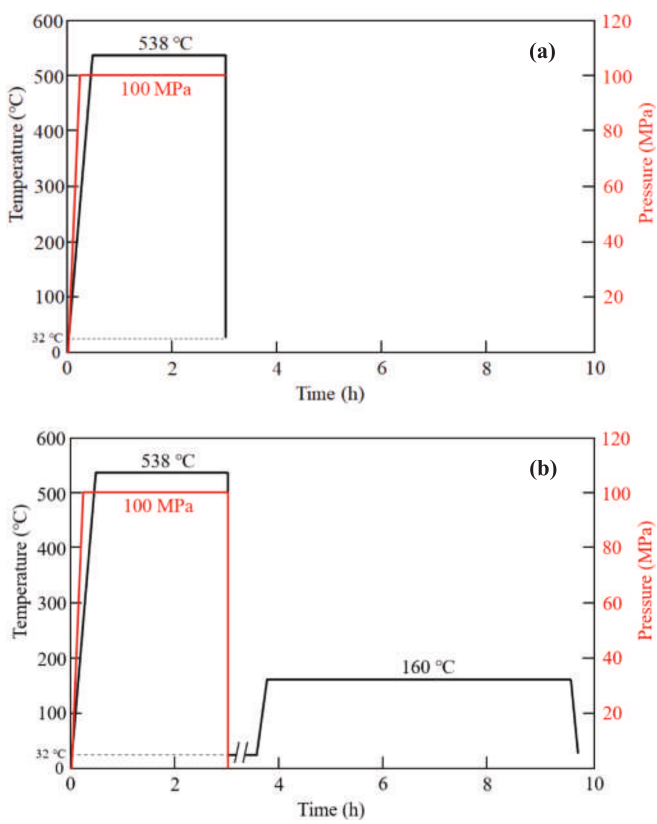

Fig. 2. Schematic representation of the two heat treatments: (a) HPHT^{TM}, (b) HPHT^{TM} + Aged.

Table 1
HPHT^{TM} solution-age thermal process parameters.

Process	Temperature	Pressure	Time
HIP/Solution	538°C ± 6°C	100 MPa ± 3 MPa	3 h ± 15 min
Gas Quench	32°C	100 MPa ± 3 MPa	N/A
Age	160°C	0.1 MPa (Atmospheric)	6 h ± 15 min

alloys, the rapid solidification rates inherent to the PBF-LB process refine the grain structure and promote a more uniform distribution of silicon particles and Mg_2Si precipitates [4,5]. This results in improved strength, fatigue resistance, and surface quality compared to conventionally cast counterparts [6,7].

Unlike cast Al-Si materials, the material produced by PBF-LB contains process-induced defects such as porosity, lack of fusion, keyhole, surface roughness, and residual stresses, all of which significantly affect fatigue performance, limiting the use in demanding industries [8–10]. Therefore, post-processing treatments such as surface processing, heat treatment, and hot isostatic pressing (HIP) are often required to tailor the microstructure, improve the density of the printed parts, and/or enhance the surface quality [11,12].

Sole T6 heat treatment (solutionizing followed by quenching and artificial aging) of PBF-LB AlSi7Mg has been shown to reduce the strength and fatigue performance due to coarsening of Si particles and diffusion-driven growth of pores [13–15]. Similarly, HIP-only treatment, although effective at collapsing internal volumetric defects and increasing part density, does not provide meaningful precipitation strengthening. The high-temperature hold during HIP promotes coarsening of the Si network and causes dissolution or over-aging of Mg_2Si- and iron-rich precipitates, leaving the alloy in a softened condition. To restore and enhance mechanical performance, a subsequent aging treatment is required to reintroduce fine, uniformly distributed strengthening precipitates. Thus, while both sole T6 and HIP-only treatments have limitations, combining HIP with post-HIP aging (e.g., a full T6 cycle) is essential for achieving the desired strength and fatigue resistance. It is also important to note that heat treatments such as T6 can promote the nucleation and growth of hydrogen pores, potentially compromising the high density achieved by HIP and degrading mechanical properties.

A new heat treatment method developed by Quintus Technologies, known as high-pressure heat treatment (HPHT^{TM}), integrates both HIP and T6 heat treatment in a single step. A novel Uniform Rapid Quenching (URQ®) HIP furnace allows for HPHT^{TM} by combining the standard HIP process and T6 solution heat treatment and quench [16,17]. This innovative heat treatment can achieve both densification and hardening effects typical of T6 heat treatment, while reducing the chances of any pores re-opening [14,16]. Additionally, HPHT^{TM} offers other benefits, such as reduced processing time and lower geometric distortion of complex geometries, and because pressure is applied during

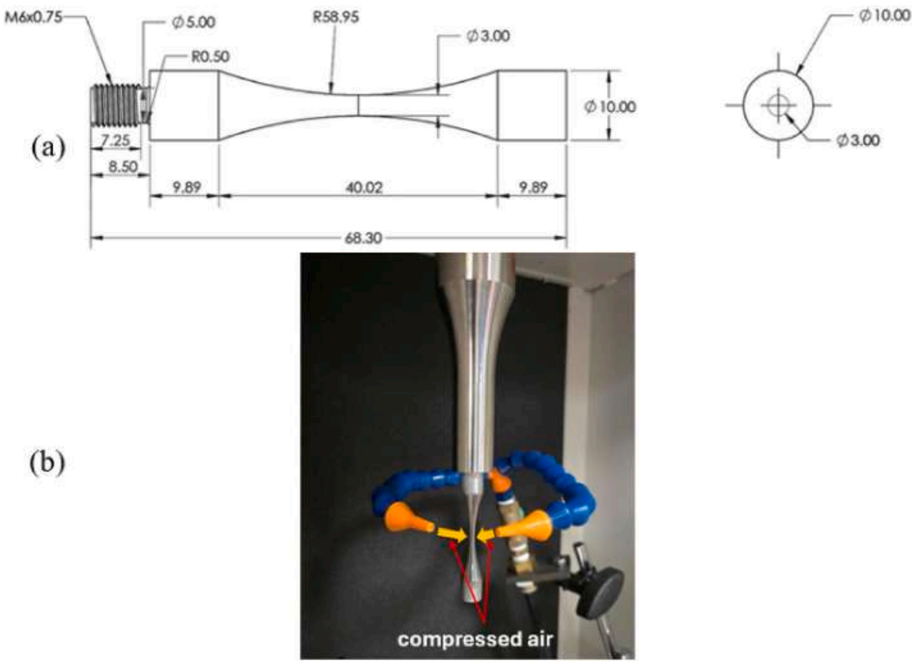

Fig. 3. (a) Hourglass specimen geometry and dimensions for USF testing of PBF-LB AlSi7Mg. All dimensions are in mm, (b) USF testing setup.

all thermal segments, hydrogen blistering can be prevented.

Understanding how the fatigue performance of the alloy can be enhanced when subjected to different post-processing treatments enables the broader industrial adoption of PBF-LB Al–Si alloys in critical applications. Limited studies have explored the effect of post-processing treatments in the high-cycle fatigue (HCF) regime and very high-cycle fatigue (VHCF) of PBF-LB AlSi7Mg, and to the best of the authors' knowledge, the effect of HPHT^{TM} on VHCF performance has not been studied yet, which highlights the need for this study.

Nasab et al. [18] studied the combined effect of surface anomalies and volumetric defects on the HCF assessment of AlSi7Mg fabricated via PBF-LB and found that both surface anomalies (such as roughness) and volumetric defects (such as internal pores) significantly influence the fatigue behaviors of the additively manufactured AlSi7Mg alloy. In a subsequent study, Nasab et al. [19] investigated the fatigue behavior of additively manufactured laser shock peened AlSi7Mg alloy and reported that the post-processing method improved the fatigue life when compared to the as-built parts. Martins et al. [20] studied the effect of platform temperature combined with a T5 heat treatment on the HCF response of AM AlSi7Mg. Understanding how the fatigue performance of the alloy can be enhanced when subjected to different post-processing treatments enables the broader industrial adoption of PBF-LB Al–Si alloys in critical applications of AlSi7Mg alloy, and found improved fatigue life of the T5 specimens. Liu [21] showed that process-induced microstructural anisotropy plays a critical role in the fatigue crack growth mechanism. Zhao et al. [22] investigated the VHCF behavior and ultra-slow crack propagation behavior of PBF-LB AlSi7Mg alloy under as-built conditions, but the effect of any post-heat treatment was not studied. Tusher and Ince [8] investigated the influence of T6 heat treatment on the VHCF response of PBF-LB AlSi7Mg alloy (relative to the as-built counter material) and found that the T6 heat treatment reduces VHCF strength. They, however, did not study the effect of HIP and HIP + T6 on the mechanical properties and VHCF response of the alloy.

This study aims to evaluate the VHCF performance of the PBF-LB AlSi7Mg alloy upon applying a novel HPHT^{TM} that integrates HIP and heat treatment along with a separate T6 aging cycle. The objective of this study is to investigate VHCF behavior and compare it with the as-built condition, and quantify the controlling mechanism(s) of VHCF crack initiation. The novelty of the work lies in the application of a time-efficient HPHT^{TM} cycle, which consolidates densification and heat treatment in one step, to PBF-LB Al–Si alloys, a heat treatment approach not yet explored for VHCF performance, not only in cast AlSi7Mg but also in any PBF-LB Al–Si alloys. This study contributes to a more widespread industrial use of PBF-LB AlSi7Mg alloy in critical applications where components could be exposed to an extended number of cyclic loadings beyond 10 million cycles. To this end, there is a critical gap in understanding the fatigue behavior of PBF-LB AlSi7Mg alloy in the VHCF regime and how the HPHT^{TM} process influences the VHCF performance with attention to microstructural evolution, although previous studies have studied the VHCF of PBF-LB AlSi7Mg in the as-built state [8,22] and conventional T6 aged condition [8]. This study seeks to add important new understanding to the existing knowledge base and expand the safe application of additively manufactured AlSi7Mg in critical engineering applications.

2 . Experimental Procedure

2.1 . Starting material

The powder used in the Selective Laser Melting (SLM) Metal 3D Printer was gas-atomized AlSi7Mg powder supplied by IMR Metal Technologies (Frankfurt am Main, Germany). The chemical composition of the powder is (Si: 7.10 %, Mg: 0.56 %, Fe: 0.08 %, Ti: 0.07 %), and the powder is mainly spherical with a particle size distribution (PSD) of D10: 26.4 µm, D50: 39.7 µm, and D90: 59.7 µm.

The SLM 280HL system was employed to fabricate cylindrical samples made of AlSi7Mg alloy. The fabrication process employed processing parameters, including a scanning speed of 1200 mm/s, a laser power of 370 W, a hatch spacing of 190 µm, a layer thickness of 30 µm, a laser spot diameter of 0.100 mm, and an inert gas flow rate of 3 L/min. The build plate was maintained at a temperature of 100 °C throughout fabrication. Cylindrical specimens with a diameter of 12 mm and height of 80 mm were produced in a vertical build orientation, as shown in Fig. 1(a), such that the build direction coincided with the direction of fully reversed tension–compression cyclic loading. The layer-wise scan pattern employed a 67° rotation between successive layers (i.e., the scan vector was rotated by 67° from one layer to the next); Fig. 1(b). To reduce contamination and prevent defects arising from external

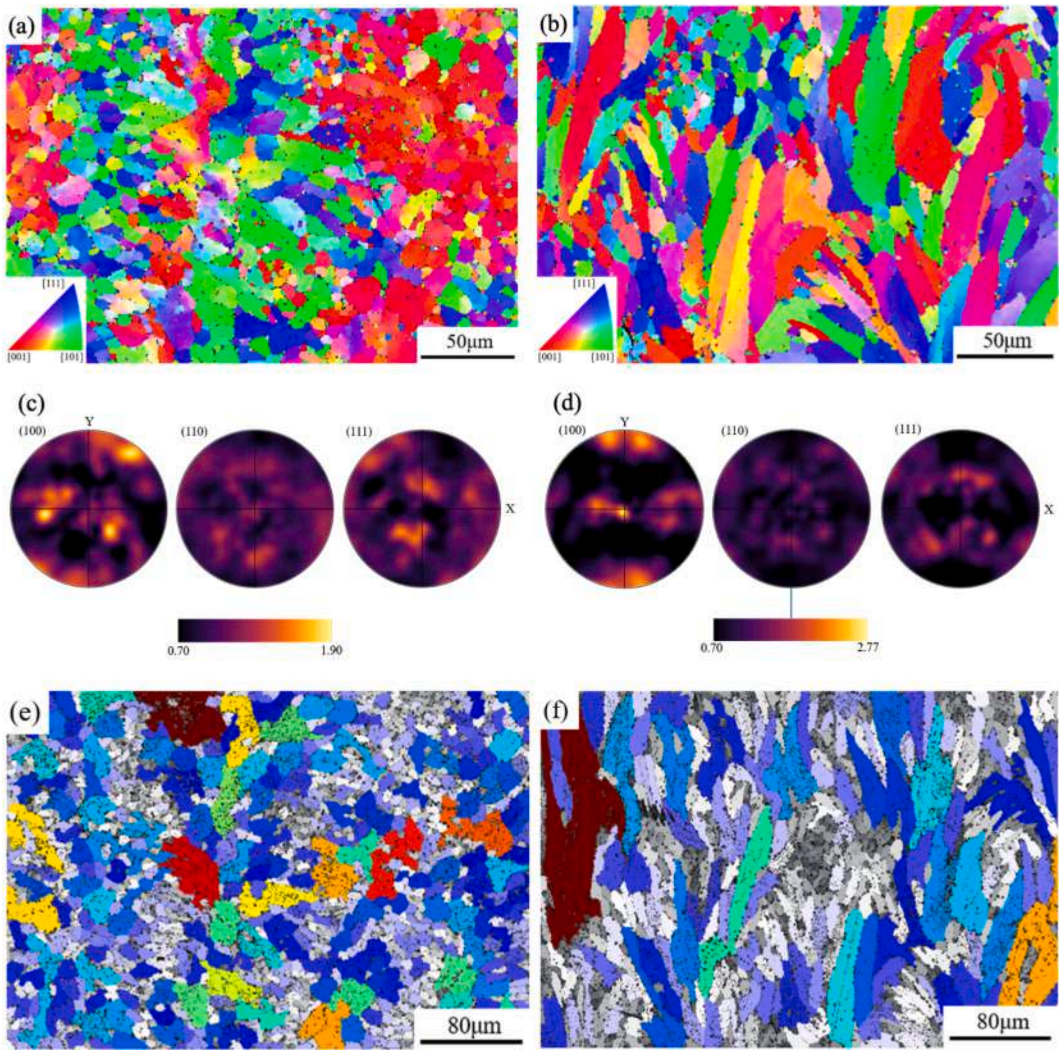

Fig. 4. EBSD images of HPHT^{TM} PBF-LB AlSi7Mg: (a, c, e) XY plane showing fine grain structure with uniform distribution; (b, d, f) XZ plane showing large columnar grains. (a, b) Inverse pole figure (IPF) maps; (c, d) pole figures; (e, f) grain size maps.

impurities, argon gas was continuously used during the entire manufacturing process. A total of 21 cylindrical samples were fabricated for this study. After printing, the deposited cylindrical samples were cut from the substrate and heat-treated.

2.2. Heat treatment

PBF-LB AlSi7Mg cylindrical samples were heat treated with an HPHT^{TM} strategy at Quintus Technologies Application Center (Columbus, OH), which combines HIP, solution heat treatment, and quenching all in the same HIP vessel under high pressure with the use of a URQ furnace. At the end of the HIP (538 °C ± 6 °C) at 100 MPa, samples were directly gas quenched with a quenching rate greater than 2000 °C /min with Argon until the cylindrical samples reached 32 °C. Artificial aging at a lower temperature was not suitable to be performed in the same HIP furnace due to the thermocouple types being used for the control. Hourglass specimens for ultrasonic fatigue (USF) testing were machined down from the cylindrical samples after HPHT^{TM}. Artificial aging of the hourglass specimens was performed in a separate heat furnace at 160 °C for 6 h. A schematic representation of two heat treatments is shown in Fig. 2, and the process parameters are shown in Table 1. A total of 21 fatigue specimens underwent HPHT^{TM} treatment, of which 8 fatigue specimens were artificially aged.

2.3 . Microstructure analysis and fractography

Scanning electron and transmission electron microscopy (SEM and TEM) were utilized for high-resolution imaging to quantify the size, shape, and morphology of the ultrafine grains and precipitates. The grain structure and texture were investigated through electron backscatter diffraction (EBSD) analysis, and the chemical composition of the fine precipitates was analyzed through TEM-based energy dispersive spectroscopy (EDS).

SEM imaging and EBSD analyses were performed using a Thermo Fisher Scientific Helios 5 PFIB CXe SEM equipped with an Oxford Instruments Symmetry S3 EBSD detector. Backscattered electron (BSE) imaging was conducted at 5 kV, while EBSD data were acquired at 20 kV. Map and step sizes were optimized to capture global and local microstructures. EBSD maps in a size of 270 × 180 μm were collected with a step size of 0,5 μm. EBSD data processing was performed using the Hough transform and the Aztec software. EBSD data were further analyzed with ATEX software to generate inverse pole figures (IPF) and grain size distribution plots [3,23]. Samples for SEM and EBSD analysis were mechanically ground on water abrasive papers, polished using diamond suspension, and finally polished using vibrational polishing on silica suspension.

TEM analysis was performed using an FEI Tecnai TF20 X-TWIN field emission gun microscope operating at 200 kV. Thin foils were prepared

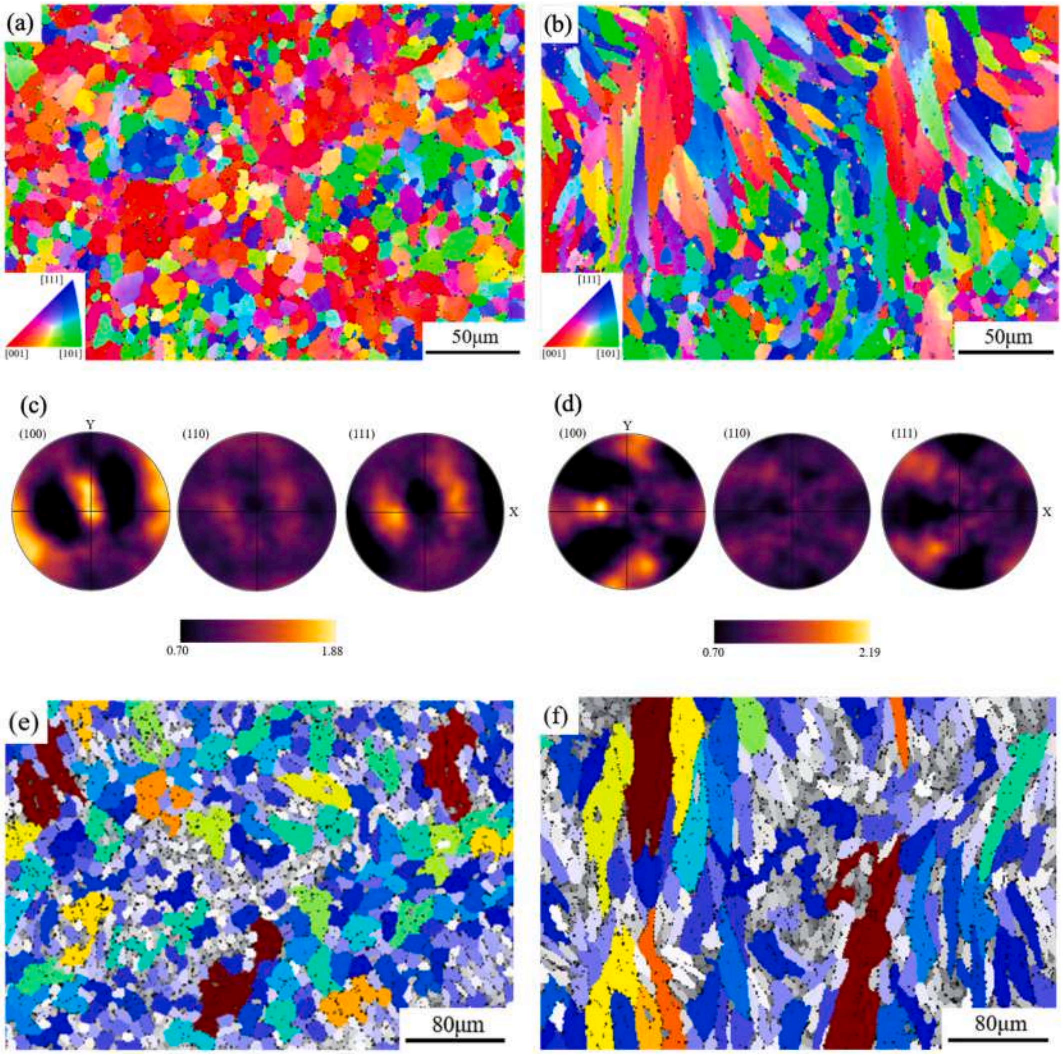

Fig. 5. EBSD images of HPHT^{TM} + Aged PBF-LB AlSi7Mg: (a, c, e) XY plane showing fine grain structure with uniform distribution; (b, d, f) XZ plane showing large columnar grains. (a, b) Inverse pole figure (IPF) maps; (c, d) pole figures; (e, f) grain size maps.

by grinding to ~ 100 μm thickness, followed by twin-jet electropolishing in a 30 % HNO3 methanol solution at − 35 °C using a Struers TenuPol system. High-resolution TEM (HR-TEM), high-angle annular dark field (HAADF) imaging, bright field (BF) imaging, selected area electron diffraction (SAED), and EDS were conducted to obtain detailed insight into microstructure [3,23].

The post-mortem fractography analysis was conducted to quantify crack initiation, crack propagation, and final fracture using a two-step characterization approach. Initial observations were performed using a Keyence VHX-600 digital microscope at low magnification to identify overall fracture morphology (crack initiation location, crack propagation region and final overload fracture region). Then, SEM with an FEI Quanta 3D FEG System was used for the detailed examination of the fractured surface.

2.4 . Porosity analysis

A 3D porosity analysis was performed at the gauge section of the hourglass fatigue specimens using custom-built X-ray computed tomography (XCT) at the J-Tech@PoliTO laboratories to examine the three-dimensional distribution of defects and to characterize the pore morphology and size variation within the two specimens (HPHT^{TM} and HPHT^{TM} + Aging) of PBF-LB AlSi7Mg. For porosity analysis, an ≈ 80 mm^3 from the middle of the gauge section of one of each sample's configuration was scanned. The scanned section was roughly 10 mm along the specimen's longitudinal axis. The parameters of the scans were 180 kV and 70 μA, resulting in a nominal power of 12.6 W. A physical copper filter of 0.2 mm was used to filter out low-intensity radiation to enhance the quality of the final 3D reconstruction. The specimen was placed 35 mm from the X-ray source, and the detector was placed at 1300 mm from the X-ray source, achieving a voxel size resolution of ≈ 5.5 μm. A total of 1600 2D projections were acquired during the tomography acquisition. The 3D volumes were reconstructed using VG MAX 3.5 software (Volume Graphics GmbH, Heidelberg, Germany) using a filter back projection algorithm. By means of the porosity/inclusion module of VG Studio software, the defects were characterized by filtering out the defect with a radius of 2 voxels to avoid considering artefacts coming from the tomographic reconstruction.

2.5. Mechanical testing

Uniaxial tensile tests were conducted on all specimens using a 100 kN MTS Landmark servo-hydraulic testing machine. All tensile specimens were machined in accordance with ASTM E8 standard specifications. The tests were carried out under displacement control at a strain rate of 10^{-3} /s. The reported mechanical properties represent the average values obtained from three tests for each material condition. Mechanical properties were extracted from the individual stress–strain responses of

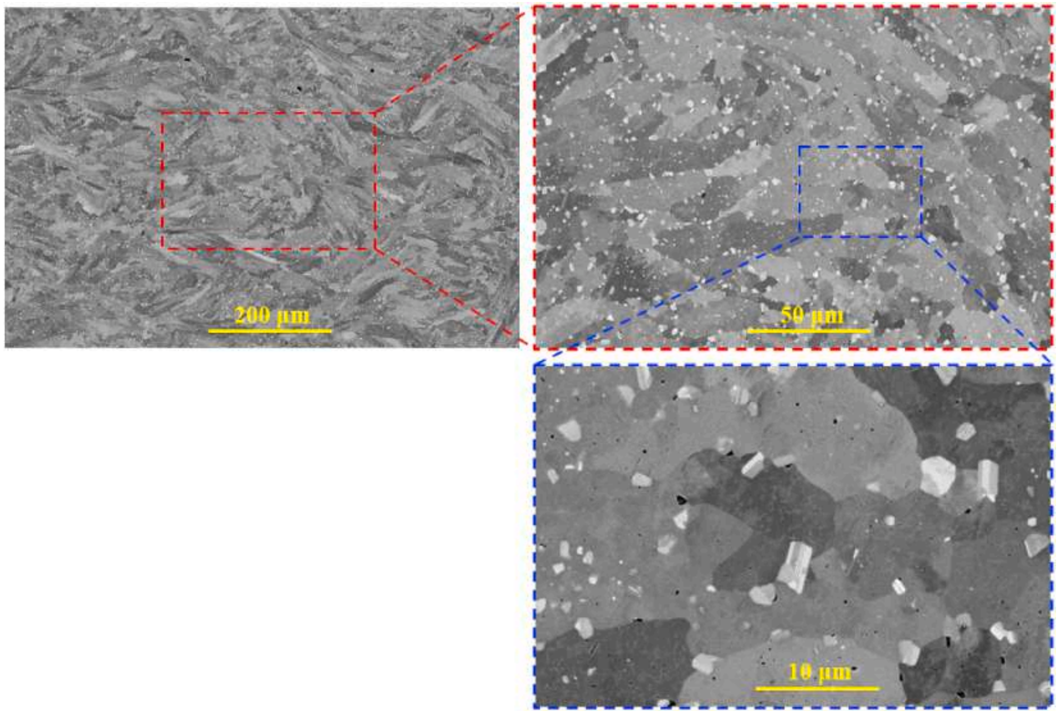

Fig. 6. SEM-BSE images of HPHT^{TM} PBF-LB AlSi7Mg in different magnifications.

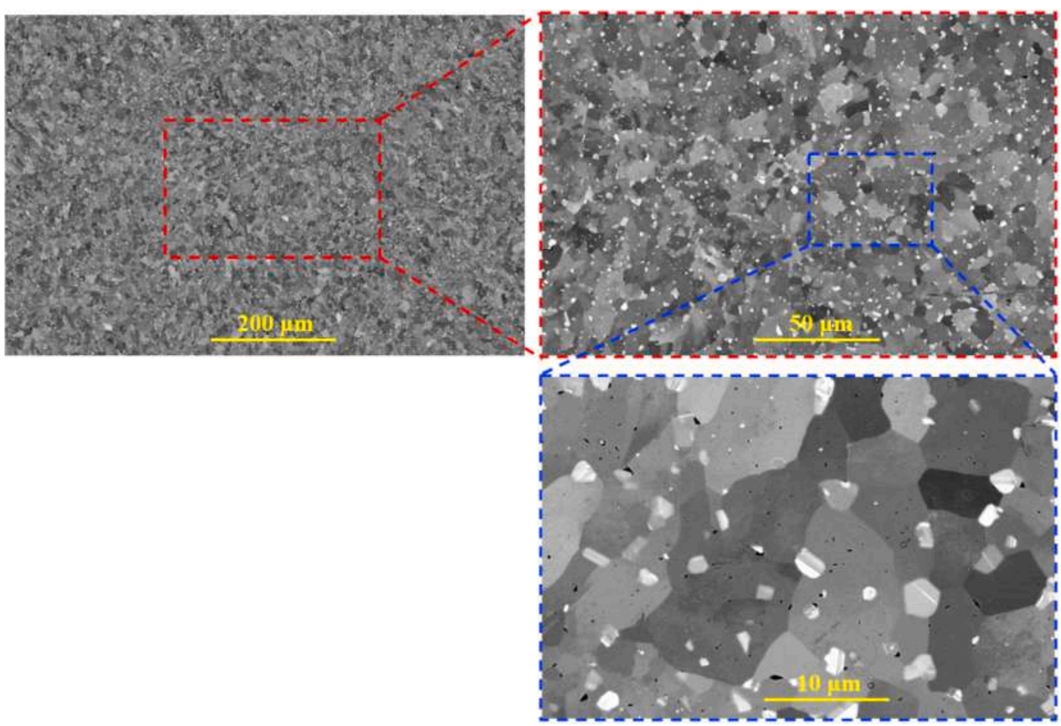

Fig. 7. SEM-BSE images of HPHT^{TM} + Aged PBF-LB AlSi7Mg in different magnifications.

each specimen, while the yield stress was determined using the conventional 0.2 % offset method.

2.6 . Ultrasonic fatigue (USF) testing

Fatigue behavior beyond 10^7 cycles, corresponding to the VHCF regime, was evaluated using a Shimadzu ultrasonic fatigue testing system (USF-2000A), operating at a frequency of 20 kHz, which enables rapid fatigue testing within a reasonable timeframe [24]. Fatigue tests were conducted on 13 HPHT^{TM} heat-treated specimens and 8 HPHT^{TM} heat-treated with artificially aged. Tests were conducted under fully reversed conditions, with a stress ratio (R) of −1 at an ambient temperature. The hourglass-shaped specimens (Fig. 1(c)) were designed considering AlSi7Mg alloy's Young's modulus (68 GPa) and density (2.58 g/cm^3) to achieve a natural frequency of 20 kHz (specimen geometry and dimensions are provided in Fig. 3(a)). To eliminate surface

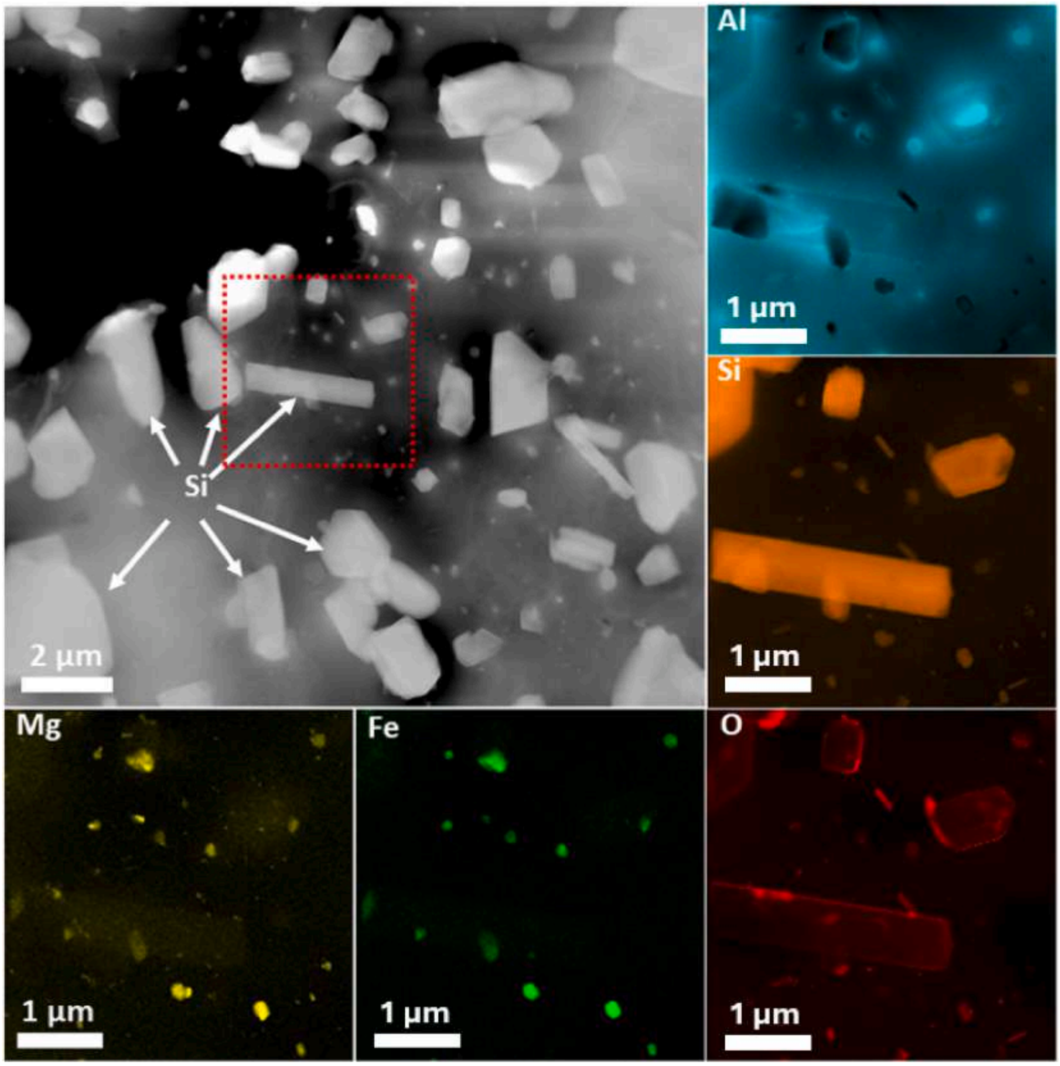

Fig. 8. HAADF-STEM image of the HPHT^{TM} microstructure. The region of interest marked by the red rectangle corresponds to the area shown in the EDS elemental maps of Al, Si, Mg, Fe, and O.

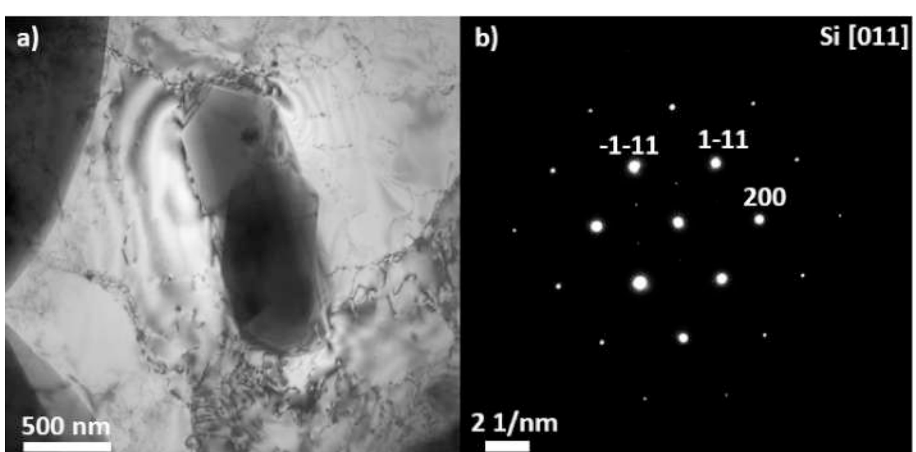

Fig. 9. a) BF TEM image of an intragranular Si particle in the HPHT^{TM} alloy; b) SAED pattern from the Si particle acquired along the [011] zone axis.

roughness effects, all machined specimens were meticulously polished using silicon carbide sandpapers ranging from 400 to 7000 grit to achieve a scratch-free surface with a mirror finish. Compressed air (Fig. 3 (b)) was continuously directed at the gauge section to dissipate heat and prevent temperature rise, while an intermittent loading sequence (300 ms pulse, 200 ms pause) was applied to further limit self-heating. The applied stress amplitudes were selected based on an earlier study of this alloy done by Tusher and Ince [8]. Fatigue failure was identified by

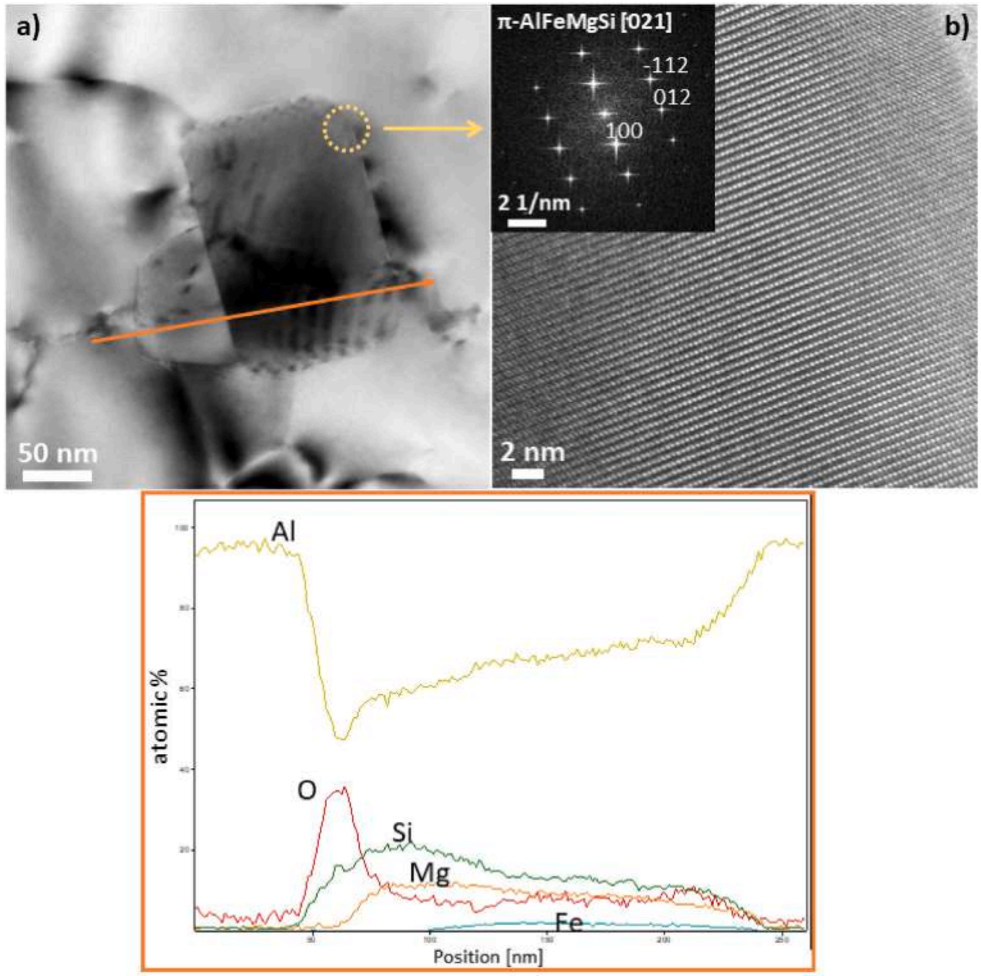

Fig. 10. a) BF TEM image of a π-phase and o-rich particles (HPHT™); b) HRTEM image of a π-phase with FFT insect, area marked by a dashed yellow circle in a). An EDS line scan along the orange line in (a) is also included in this figure.

monitoring the resonance frequency, where a decrease to 19.5 kHz indicated specimen failure. Additionally, the runout for the VHCF testing was set to 10^9 cycles. To ensure the results are reliable and consistent, at least two specimens are tested at each stress level. This repetition helps confirm that the observed behavior is repeatable and that the data accurately reflects the specimen's performance under different conditions. Following the fatigue tests, fractographic analysis was conducted using a Keyence VHX-600 Digital Microscope and an FEI Quanta 3D FEG SEM to investigate crack initiation and propagation mechanisms in the VHCF domain.

3. Results and discussion

3.1. Microstructural analyses

EBSD analysis was performed on samples under both HPHT™ and HPHT™ + Aged treatments in cross sections perpendicular to the build direction (XY plane) as well as in sections parallel to the build direction (XZ plane), providing in-depth insights into the material's grain size, grain distribution, and crystallographic texture, highlighting the microstructural characteristics of the PBF-LB AlSi7Mg alloy studied in this research. Figs. 4 and 5 show the EBSD data (grain orientation, size distribution, and crystallographic texture) of HPHT™ and HPHT™ + Aged materials in the XY and XZ planes, respectively. The texture analysis of the XY and XZ planes, illustrated in the inverse pole figure (IPF) maps (Fig. 4a, b & 5a, b) and the corresponding pole figures (Fig. 4c, d & 5c, d), reveals a relatively weak texture intensity with a modest preference in the $< 100 >$ crystallographic direction for both HPHT™ and HPHT™ + Aged samples. Fig. 4e & f (HPHT™ condition) and Fig. 5e & f (HPHT™ + Aged condition) show the grain structure and size distribution of PBF-LB AlSi7Mg in the XY and XZ planes, respectively, revealing distinct variations in grain morphology and orientation.

In the XY plane (Fig. 4e & 5e), a fine, equiaxed grain structure with a uniform spatial distribution is observed under both conditions. The average grain size slightly increases, measured at 14.36 ± 10.55 μm (20.75 ± 7.21 μm) for the HPHT™ sample and 16.22 ± 10.23 μm (21.57 ± 7.54 μm) after aging. The average grain size for both samples indicates a relatively fine-grained structure, which can influence the material's mechanical properties, such as fatigue resistance, toughness, and strength. Conversely, the XZ plane (Fig. 4f & 5f) shows coarser, elongated columnar grains oriented roughly along the build direction (Z). The average grain slightly increases, measured at 25.27 ± 22.45 μm (55.40 ± 19.87 μm) for the HPHT™ sample and 27.23 ± 20.27 μm (65.40 ± 21.56 μm) after aging. This coarse columnar morphology indicates epitaxial grain growth through successive layers influenced by the directional heat flow inherent to the PBF-LB process [25–27].

The as-built microstructure of PBF-LB AlSi7Mg consists of an ultra-fine cellular/dendritic α-Al surrounded by a continuous Si-rich eutectic network formed under rapid solidification, with clearly visible melt-pool boundaries, and porosity that acts as crack-initiation sites [8]. After HPHT™, the cellular eutectic network is completely dissolved, the melt-pool structure is homogenized, and the alloy transforms into a coarser α-Al grain structure containing uniformly dispersed, spheroidized Si particles, as shown in Fig. 6 with bright contrast. Most of the porosity is

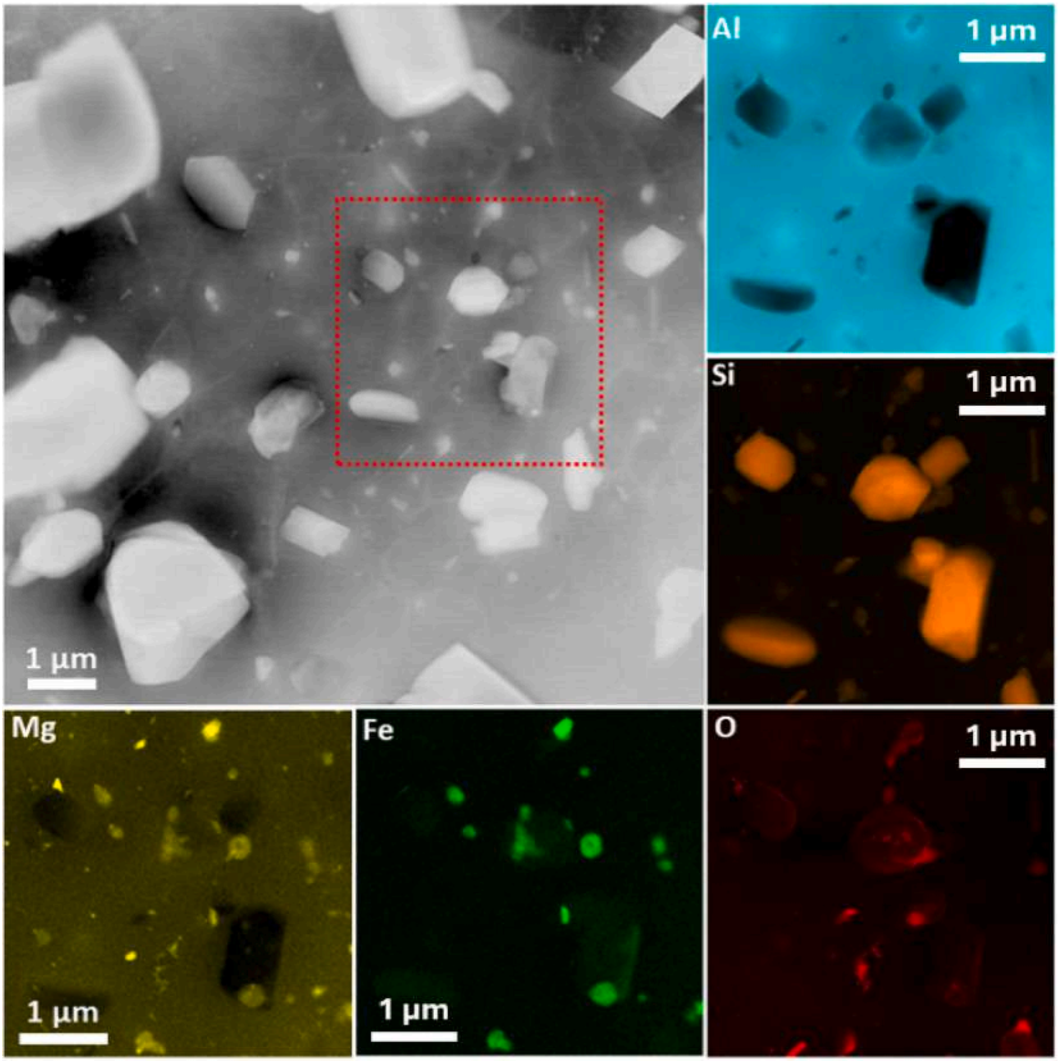

Fig. 11. HAADF-STEM image of the HPHT^{TM} + Aged PBF-LB AlSi7Mg alloy microstructure. The region of interest marked by the red rectangle corresponds to the area shown in the EDS elemental maps of Al, Si, Mg, Fe, and O.

eliminated by hot isostatic pressure, and melt-pool boundaries disappear. In the HPHT^{TM} + aged condition, as shown in Fig. 7, the distribution of coarse Si particles remains similar to the HPHT^{TM} condition, but the supersaturated α-Al matrix undergoes precipitation of fine β″, and GP-zone clusters that are not visible in SEM, but their presence is confirmed in TEM images, and they significantly enhance fatigue resistance. As a result, the microstructure evolves from a highly heterogeneous and anisotropic as-built state to a densified, homogenized microstructure, and finally to a precipitation-strengthened aged condition.

To further quantify the microstructure and the effect of the implemented heat treatments on the Si morphology, extensive scanning TEM quantifications were performed on the studied materials. Fig. 8 shows that the HPHT^{TM} microstructure of the PBF-LB AlSi7Mg alloy is dominated by discrete Si particles with characteristic dimensions ranging from several hundred nanometers to a few micrometers. The Si phase is broadly dispersed throughout the Al matrix; however, a tendency toward local clustering is observed, with frequent particle coalescence and agglomeration indicative of diffusion-assisted coarsening [28]. Si particles are preferentially located along Al grain boundaries, although some of the smaller Si particles were also observed within grain interiors. This preferential localization is consistent with enhanced diffusion and solute redistribution along grain boundaries during HPHT^{TM}, which promotes Si transport and coarsening at these interfaces [29].

The Si particle morphology is highly heterogeneous, ranging from near-equiaxed particles with partially rounded edges to elongated and strongly faceted particles with sharp edges. In projection, both polygonal and triangular cross-sections are observed depending on the sectioning plane, reflecting the crystallographic anisotropy of Si and the persistence of faceted growth/shape stabilization despite partial rounding during HPHT^{TM}.

Within the spatial resolution of EDS elemental mapping, no evidence of a continuous cellular Si network is detected, suggesting that the characteristic PBF-LB cellular architecture has been largely disrupted by HPHT^{TM}. It is consistent with diffusion-driven chemical homogenization combined with Si coarsening and particle coalescence at elevated temperature, leading to the breakdown of the fine-scale cellular framework and its replacement by a discontinuous dispersion of coarsened Si particles [30]. EDS oxygen maps reveal O-enriched shells surrounding large Si particles. While surface oxidation during TEM specimen preparation cannot be excluded, the consistent localization of oxygen at the particle–matrix interface suggests the possible presence of a thin oxide layer associated with the Si particles.

In addition to Si particles, EDS maps revealed Al–Mg–Si–Fe-rich intermetallic particles in the HPHT^{TM} alloy. A moderate density of dislocations within the Al matrix that are locally concentrated in the vicinity of Si particles is observed (Fig. 9a) and at grain boundaries, suggesting that thermal mismatch strains and particle–matrix

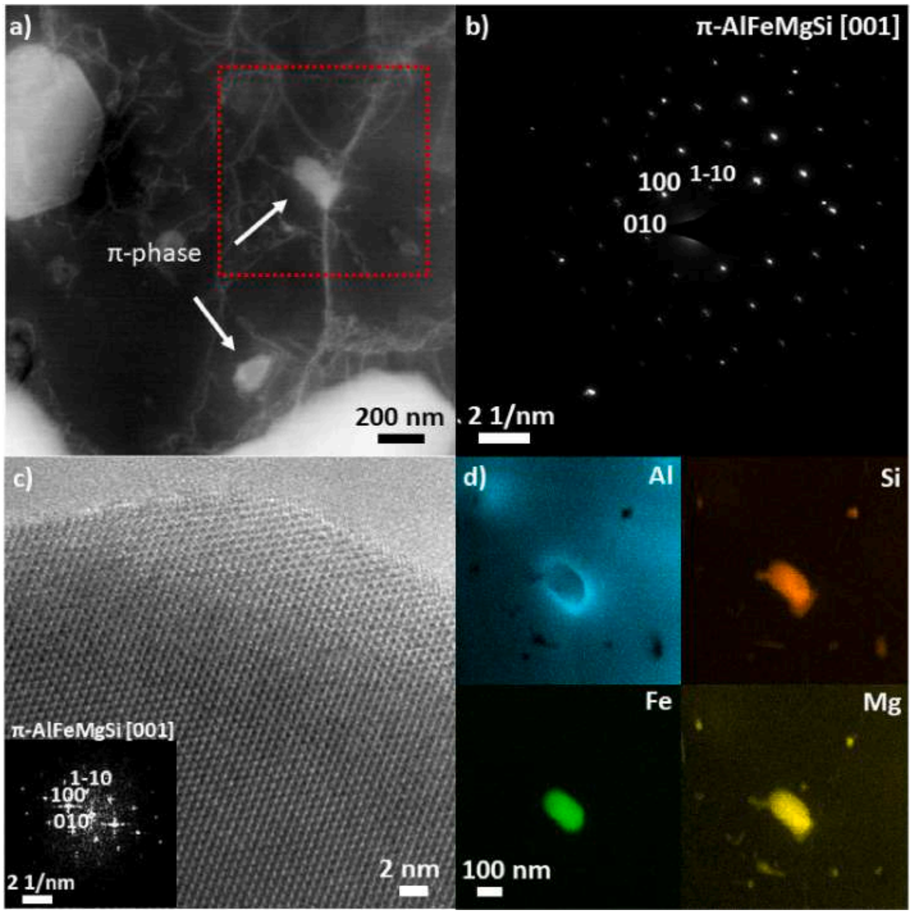

Fig. 12. a) HAADF-STEM image of the HPHT^{TM} + Aged alloy; b) SAED pattern acquired from a π-phase particle along the [001] zone axis; c) HRTEM image of a π-phase particle with the corresponding FFT shown as an inset; d) STEM–EDS elemental maps of the π-phase particle, the mapped area is indicated in a) by the red dashed square.

interactions contribute to dislocation storage after HPHT^{TM}. Phase identification based on Fast Fourier Transform (FFT) patterns obtained from High Resolution Transmission Electron Microscope (HRTEM) images (Fig. 9b) is consistent with the π-phase ($Al_8Mg_3FeSi_6$), suggesting the presence and possible stabilization of Fe-bearing intermetallics during HPHT^{TM}. The occurrence of the π-phase is consistent with previous reports on Fe-containing Al–Si–Mg alloys, in which π (Al–Mg–Fe–Si) intermetallics are commonly observed after high-temperature processing [31,32]. Fine O-rich particles with Si–O and Mg–Si–O enrichment were also detected by EDS in the HPHT^{TM} condition, occasionally attached to π-phase intermetallics (Fig. 10). These particles are likely oxide/oxide–silicate inclusions; however, their small size prevented unambiguous diffraction-based identification.

At first inspection, the microstructure of the alloy after HPHT^{TM} + Aged treatment (Fig. 11) appears comparable to that observed in the HPHT^{TM} state. Coarse, discrete Si particles continue to dominate the microstructure, with characteristic dimensions ranging from several hundred nanometers to a few micrometers. The Si phase is distributed throughout the Al matrix, and no evidence of a continuous cellular Si network is detected. Like the HPHT^{TM} condition, EDS maps frequently reveal an oxygen-enriched shell surrounding the Si particles, suggesting the presence of a thin oxide layer at the particle–matrix interface and/or surface oxidation effects associated with specimen preparation.

HPHT^{TM} + Aged material, like the HPHT^{TM} sample, contains well-dispersed Al–Si–Mg–Fe-rich intermetallics with typical sizes of ~ 50–200 nm, which are observed throughout the matrix. Electron diffraction and FFT analysis (Fig. 12) indicate that these particles are consistent with the π-phase, supporting the persistence of Fe-bearing intermetallics after HPHT^{TM}. In addition, nanoscale O-rich particles enriched in Si and/or Mg are detected by EDS. Overall, the secondary phases exhibit a relatively homogeneous dispersion, indicating that the HPHT^{TM} + Aged treatment promotes a chemically equilibrated microstructure with a stable distribution of coarsened Si particles and fine intermetallic/oxide-based particles.

While the Si particles and Fe-bearing intermetallics remained largely unchanged, higher-magnification TEM observations revealed fine needle-like precipitates within the Al grains. Fig. 13. shows the TEM micrographs taken along the < 100 > Al axis showing the needle-like nanoscale precipitates in the α-Al matrix after HPHT^{TM} + Aged treatment (i.e., BF TEM image (Fig. 13a), HRTEM images (Fig. 13b & d), FFT of a needle-like precipitate (Fig. 13c). In the FFT (Fig. 13c), reflections associated with the precipitates appear as streaks aligned with the $\langle 001\rangle_{Al}$, consistent with the needle-like morphology of β″ precipitates and their alignment along with Al matrix [33,34]. The precipitates with lengths of ~ 5–15 nm were predominantly observed; however, occasional longer needles up to ~ 30 nm were also present (Fig. 13d). FFT analysis indicated that these features are still consistent with β″-type precipitates. These fine needle-like β″ precipitates are the primary strengthening phase in Al–Si–Mg alloys after T6, providing significant precipitation hardening by impeding dislocation motion in the Al matrix [35]. β″ precipitates are coherent (or strongly semi-coherent) with the α-Al lattice, creating large elastic strain fields that strongly interact with dislocations. This coherency and the very small size of β″ are why it produces high strength: dislocations must either cut the coherent precipitates (high shear stress) or bow between them (Orowan looping) [29,31,36,37], thereby substantially increasing the stress needed for

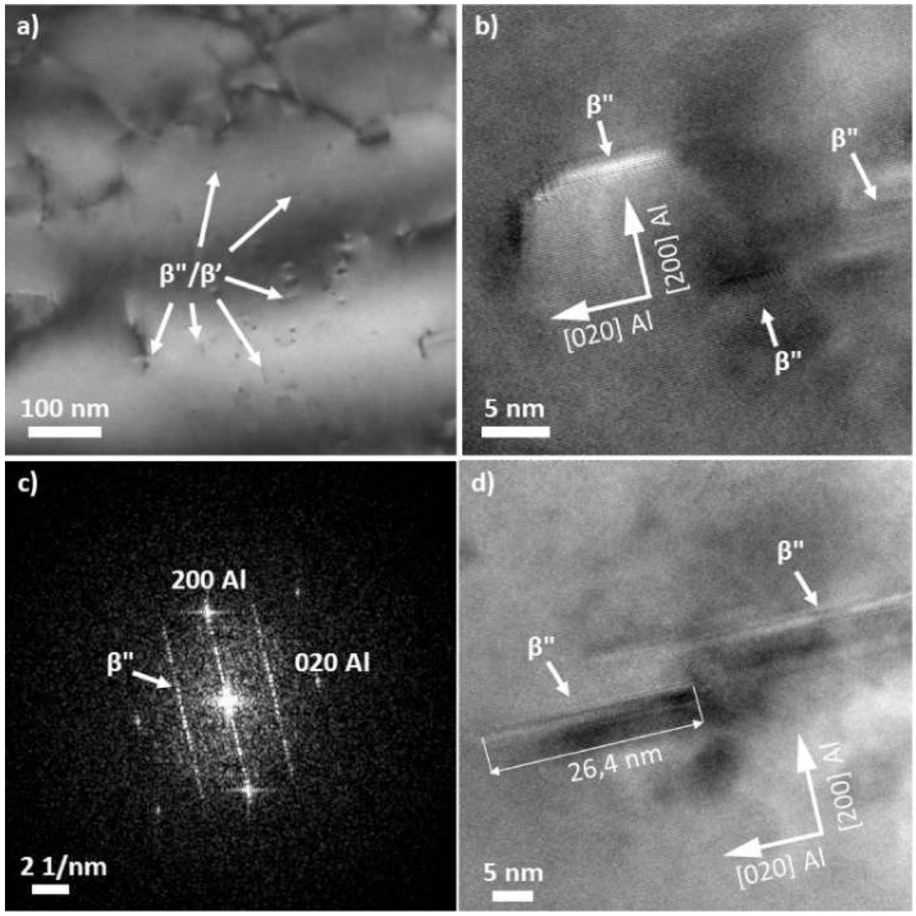

Fig. 13. TEM images taken along the <100> Al axis showing the needle-like precipitates in the α–Al matrix of the HPHT^{TM} + Aged alloy: a) BF-TEM image, b & d) HR-TEM images, c) FFT of a needle-like precipitate.

plasticity. Although β″ precipitates were detected in the post-HPHT^{TM} + Aged alloy, their density remained relatively low. Given the rapid gas quench rate (>2000 °C/min), the limited precipitation response is unlikely to result solely from inadequate quenching. Instead, it may arise from a combination of incomplete solute dissolution during HPHT^{TM} processing, solute consumption by O-rich particles or stable secondary phases, and possible pressure-induced effects on vacancy retention and precipitation kinetics, all of which could reduce the effective supersaturation available for β″ formation during aging.

After aging, a cellular dislocation substructure became evident (Fig. 14). This suggests that aging promoted dislocation rearrangement and stabilization, likely assisted by dislocation–precipitate interactions associated with the formation of fine β″ precipitates. In contrast, in the HPHT^{TM} + Aged condition, dislocations appear more diffusely distributed, consistent with recovery during HPHT^{TM} + Aged and a less organized dislocation configuration. Dislocations were frequently pinned at Si particles and π-phase intermetallics, and occasionally also near O-rich inclusions, while Orowan-type bowing was observed around the finest particles.

Fe-bearing π-phase intermetallics ($Al_8Mg_3FeSi_6$) are generally considered relatively brittle constituents in Al–Si–Mg alloys due to their limited deformability and elastic incompatibility with the α-Al matrix. Large or irregular Fe-rich intermetallics may promote local stress concentration and facilitate microcrack nucleation and propagation under cyclic loading conditions [31,32]. However, in the present study, the π-phase particles were relatively fine (~50–200 nm) and homogeneously dispersed throughout the matrix after HPHT^{TM} and HPHT^{TM} + Aged treatments (Fig. 12). Fractographic analysis did not identify these particles as dominant fatigue crack-initiation sites, as fatigue cracks consistently initiated from surface or near-surface stress concentrators. TEM observations (Fig. 14c) also suggested dislocation interactions with π-phase-containing second-phase particles, including localized pinning behavior in their vicinity, indicating that these intermetallics may also contribute marginally to local strengthening by impeding dislocation motion. Therefore, the overall fatigue behavior was governed primarily by the dissolution of the rapid-solidification cellular network, coarsening of Si particles, and the precipitation strengthening associated with β″ precipitates rather than by direct cracking of π-phase particles.

3.2. Porosity analyses

Porosity in the HPHT^{TM} and HPHT^{TM} + Aging samples was quantified by X-ray micro-computed tomography (μ-CT). For both conditions, the equivalent diameter ranges from 10 μm to 20 μm. The mean equivalent defect diameter is 13.12 μm in the HPHT^{TM} condition and decreases slightly after aging to 12.57 μm. The three-dimensional spatial distributions of the pores for the HPHT^{TM} and HPHT^{TM} + Aging conditions are reported in Figs. 15a and 16a, respectively. The size distribution histograms, instead, are plotted as a function of the square root of the projected area on the plane orthogonal to the specimen axis, which governs the fatigue failure, and are shown in Fig. 15b and 16b. Table 2 summarizes the main μ-CT defect analysis results, including the inspected volume, total porosity volume, mean equivalent defect diameter, and the sphericity index. The sphericity index is calculated as the ratio between the surface of a sphere having the same volume as the defect and the surface of the defect.

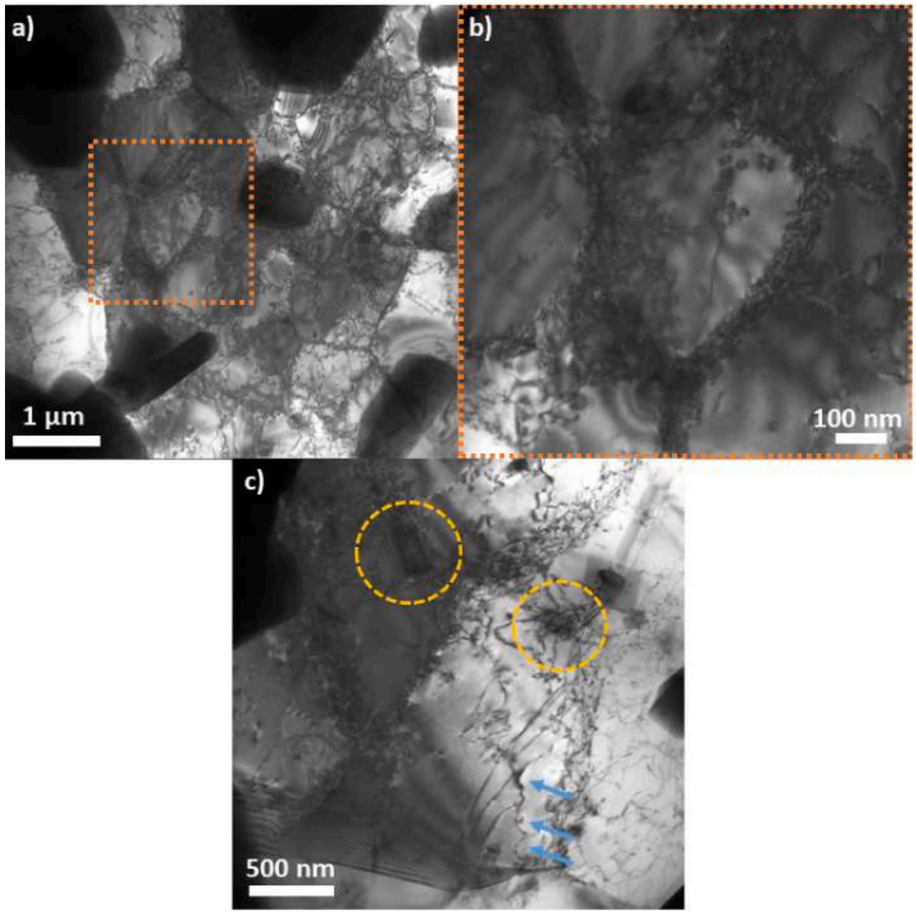

Fig. 14. BF TEM images showing dislocation structures in the HPHT^{TM} + Aged condition: a) low-magnification overview of the dislocation distribution, b) dislocation cell structure (area indicated in a) by the orange dashed square, and c) dislocation pinning around second-phase particles (yellow dashed circles) and Orowan-type dislocation bowing (blue arrows).

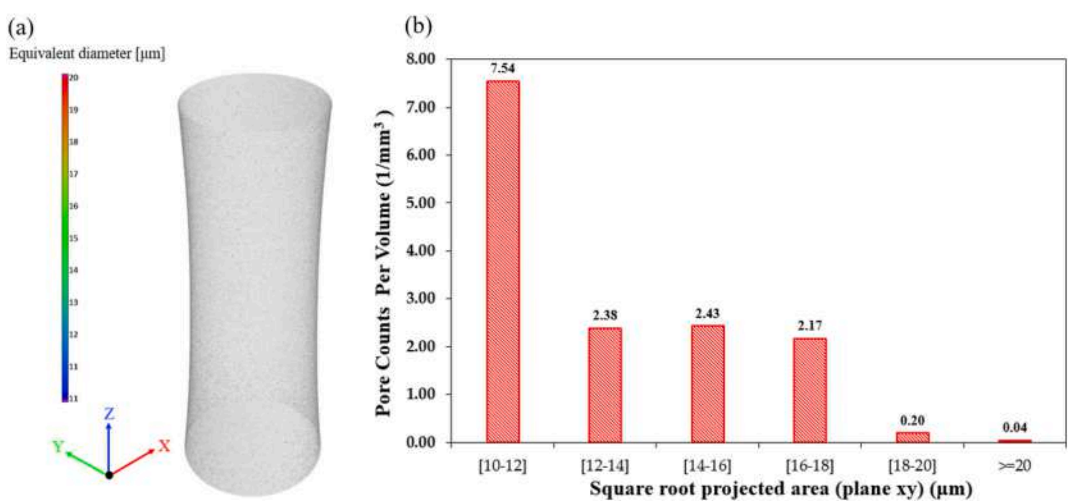

Fig. 15. CT Scan results of HPHT^{TM} PBF-LB AlSi7Mg: (a) 3D visualization of pore distribution, (b) Pore size distribution histogram.

3.3. Mechanical properties

Tensile test results of each material condition, as-built, HPHT^{TM}, and HPHT^{TM} + Aged specimens, including yield stress (YS), ultimate tensile strength (UTS), and elongation, are provided in Table 3. The tensile response of the studied PBF-LB AlSi7Mg is highly sensitive to post-processing, as is evident from the distinct stress–strain curves of the as-built, HPHT^{TM}-only, and HPHT^{TM} + Aged conditions (Fig. 17a). The as-built alloy exhibits the highest strength, while both HPHT^{TM} and HPHT^{TM} + Aged produce a noticeable reduction in strength with an increase in ductility relative to the original PBF-LB microstructure. This reduction in strength arises from a combination of thermal exposure–induced mechanisms that progressively remove the strengthening features created during rapid solidification. The as-built PBF-LB

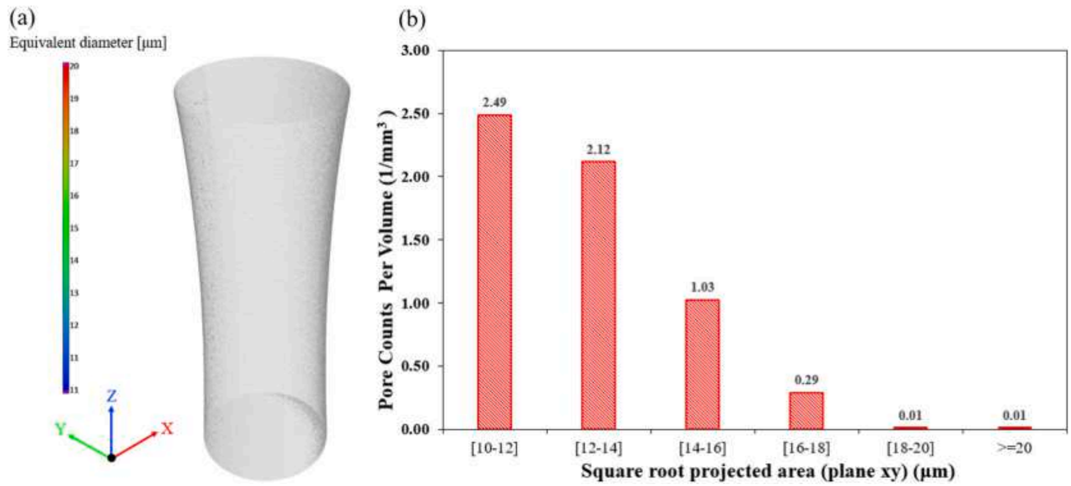

Fig. 16. CT Scan results of HPHT^{TM} + Aged PBF-LB AlSi7Mg: (a) 3D visualization of pore distribution, (b) Pore size distribution histogram.

Table 2
Summary of geometrical and porosity parameters for HPHT^{TM} and HPHT^{TM} + Aged samples from XCT analysis.

Parameters	HPHT^{TM}	HPHT^{TM} + Aged
Inspected volume (mm^3)	81	76
Porosity volume (mm^3)	2×10^{-3}	7.3×10^{-4}
Average equivalent diameter (µm)	13.12	12.57
Maximum equivalent diameter (µm)	19	20
Average sphericity index	0.62	0.61
Porosity fraction (%)	0.00247	0.00096
Relative density (%)	99.9975	99.9990

Table 3
Summary of the tensile results for PBF-LB AlSi7Mg specimens.

Materials	YS (MPa)	UTS (MPa)	Elongation (%)
As Built	266.7 ± 5.3	406.5 ± 11.2	6.2 ± 0.46
HPHT^{TM}	91.6 ± 2.4	134.5 ± 4.1	31.8 ± 2.3
HPHT^{TM} + Aged	124.6 ± 3.8	191.7 ± 4.9	24.4 ± 1.5

AlSi7Mg microstructure is characterized by an ultrafine cellular microstructure that consists of continuous eutectic Si networks in the supersaturated α-Al matrix. The eutectic Si network is built from pure Si particles that are exceptionally small and densely clustered. After the samples are treated with HPHT^{TM}, the original eutectic Si network is entirely broken down, and the characteristic cellular α-Al structure disappears. This results in significant coarsening of the Si particles compared with the as-built condition. Si particles grew through the Ostwald ripening phenomenon, forming larger, irregularly shaped Si particles that are predominantly located at grain boundaries and interfaces between aluminum grains [38]. Also, the release of solid-solution supersaturation and the relaxation of residual stress play important roles in reducing the strength of the post-heat-treated material relative to the as-built condition. Consequently, the as-built material exhibits a higher work-hardening rate than both the HPHT^{TM} and HPHT^{TM} + aged conditions (Fig. 17b), whereas the work-hardening responses of the HPHT^{TM} and HPHT^{TM} + aged states are relatively similar.

The PBF-LB process generates a markedly refined cellular–dendritic network, with solidification rates on the order of 10^5–10^7 °C/s [39–42]. This produces a submicron substructure consisting of Si-enriched cell boundaries and an Al-rich cellular interior. During HPHT^{TM}, conducted at 538 °C for extended times, this metastable architecture becomes thermally unstable. The melt-pool boundaries and the internal cell

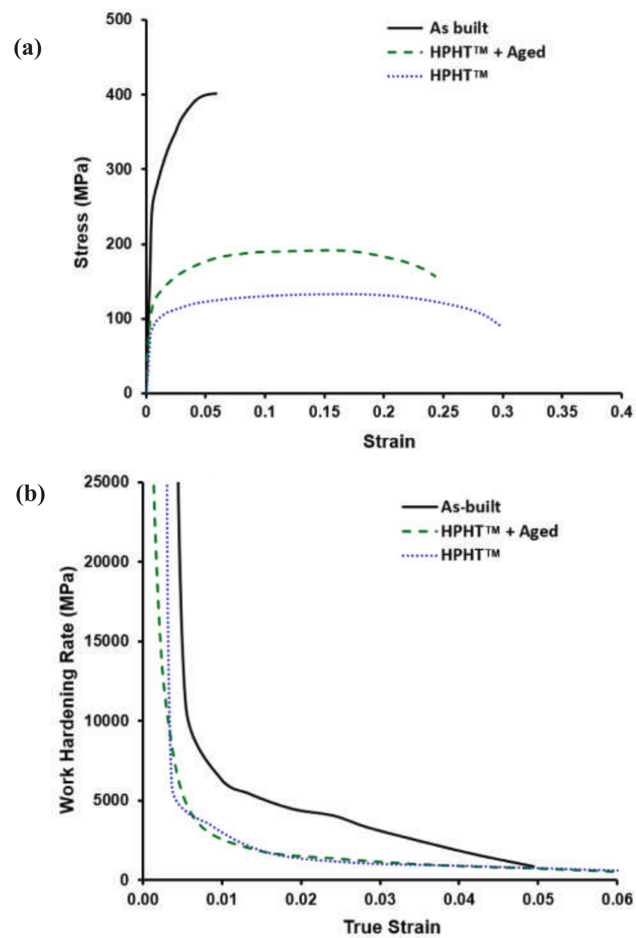

Fig. 17. a) flow curves of the studied PBF-LB AlSi7Mg , b) work hardening rate (θ) *vs.* true strain.

structure coarsen substantially, sub-grain boundary density decreases, and the originally interconnected Si-rich features transform into larger, more spheroidized particles. Since these boundaries were strong barriers to dislocation motion, their coarsening significantly reduces both yield strength and work-hardening capacity.

A second major contributor to strength loss is the disruption of the fine eutectic Si network. In the as-built state, Si is present as a

Table 4
Summary of fully reversed (R = -1) USF test data for PBF-LB AlSi7Mg specimens.

No.	Sample ID	Heat Treatment	Stress (MPa)	Number of Cycles
1	S1	HPHT™	77.5	7.61×10^8
2	S2	HPHT™	77.5	5.46×10^8
3	S3	HPHT™	80.0	2.15×10^8
4	S4	HPHT™	82.5	9.87×10^7
5	S5	HPHT™	85.0	3.51×10^7
6	S6	HPHT™	85.0	7.21×10^7
7	S7	HPHT™	90.0	1.71×10^7
8	S8	HPHT™	95.0	1.49×10^7
9	S9	HPHT™	95.0	1.52×10^7
10	S10	HPHT™	97.5	6.52×10^6
11	S11	HPHT™	97.5	6.77×10^6
12	S12	HPHT™	100	5.97×10^6
13	S13	HPHT™	120	5.00×10^4
14	S14	HPHT™ + Aged	77.5	8.12×10^8
15	S15	HPHT™ + Aged	80.0	8.18×10^8
16	S16	HPHT™ + Aged	80.0	7.61×10^8
17	S17	HPHT™ + Aged	82.5	2.88×10^8
18	S18	HPHT™ + Aged	85.0	1.76×10^8
19	S19	HPHT™ + Aged	90.0	6.85×10^7
20	S20	HPHT™ + Aged	95.0	2.43×10^7
21	S21	HPHT™ + Aged	100.0	8.76×10^6

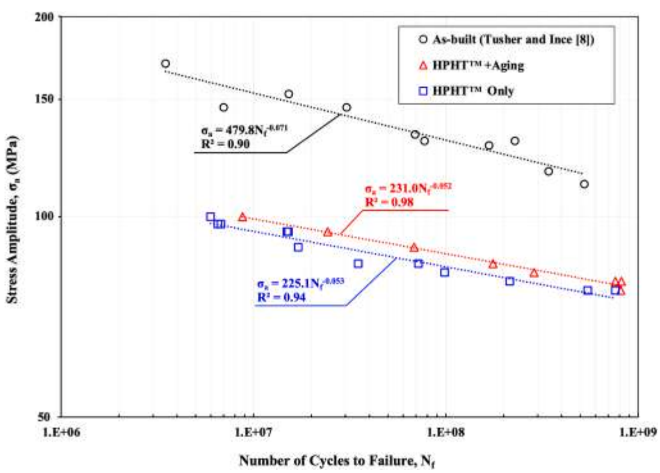

Fig. 18. VHCF S–N data of the studied materials; red triangles and blue squares represent the results of the present research, while the as-built data were reproduced from results reported in the literature [8]. To fit the Basquin lines, the runout data at 10^9 cycles have been excluded.

continuous, nanoscale eutectic framework that occupies cell boundaries and melt-pool interdendritic regions. This network plays a dual role: it provides direct strengthening through boundary pinning and indirectly enhances the mechanical stability of the cellular substructure. HPHT™ breaks down this network and replaces it with coarser, discrete Si particles that are far less effective in impeding dislocation glide. The loss of the fine-scale Si morphology, therefore, constitutes a primary mechanism of softening in HPHT™ −treated alloys.

A third factor is the reduction in solid-solution strengthening. The high cooling rates of PBF-LB trap substantial quantities of Si and Mg in supersaturated solid solution (SSSS), well above equilibrium solubility. These solute atoms strongly impede dislocation motion in the as-built condition. During HPHT™, however, both Si and Mg diffuse out of solution: Si is consumed during eutectic coarsening, and Mg is incorporated into coarse Mg–Si–bearing phases. This markedly diminishes solid-solution strengthening, removing yet another contribution to the elevated YS observed in the as-built material. Finally, PBF-LB alloys develop significant residual stress during layer-wise deposition. These stresses effectively delay the onset of macroscopic plasticity during tensile loading, contributing to the high yield strength typically measured in the as-built state. HIP relaxes nearly all these internal stresses, leaving the material in a nearly stress-free condition. Although residual stress relaxation is beneficial for dimensional stability and fatigue resistance, it simultaneously reduces the apparent tensile strength.

Despite this substantial softening, the HPHT™ + Aged condition consistently exhibits higher strength than the HPHT™ −only material. The enhancement arises from precipitation hardening activated during the HPHT™ + aging treatment, performed near 160 °C. Although HPHT™ reduces the overall supersaturation of the matrix, enough Mg and Si remain in solid solution to permit the formation of GP zones and, more importantly, β″ precipitates, the primary strengthening phase in Al–Si–Mg alloys. These fine, needle-shaped β″ precipitates introduce strong obstacles to dislocation motion and partially restore the strength lost during HPHT™. The precipitation process refines the effective slip path and elevates both yield strength and work-hardening behavior relative to the HPHT™ −only state. Nevertheless, the strength of the HPHT™ + Aged alloy does not recover to the as-built level, because precipitation cannot recreate the rapid-solidification–derived cellular network or the continuous nanoscale eutectic Si framework. Once the PBF-LB microstructure coarsens during HPHT™, the unique strengthening architecture of the as-built material cannot be reinstated. As a result, HPHT™ + Aged provides meaningful but incomplete recovery of strength by introducing a precipitation-mediated mechanism that compensates for some, but not all, of the coarsening-related losses.

3.4. S-N data

Table 4 provides a detailed overview of the ultrasonic fatigue test results for PBF-LB AlSi7Mg specimens subjected to fully reversed loading conditions (R = − 1). It lists the specimen ID, corresponding -stress amplitude, and the number of cycles to failure. Specimens with IDs from S1 to S13 are heat treated with the HPHT™ strategy only, and specimens with IDs from S14 to S21 are heat treated with the HPHT™ strategy followed by artificial aging. In all cases, crack initiation began at the surface and propagated until the final fracture.

Fig. 18 shows the VHCF S–N behavior of the as-built, HPHT™ only, and HPHT™ + Aging conditions and the corresponding Basquin fits: as-built: $\sigma_a = 479.8\,N_f^{-0.071}$ ($R^2 = 0.90$), HPHT™ only: $\sigma_a = 231.0\,N_f^{-0.052}$ ($R^2 = 0.98$), HPHT™ + Aged: $\sigma_a = 225.1\,N_f^{-0.053}$ ($R^2 = 0.94$). The as-built material has markedly higher stress amplitudes across the VHCF range despite the presence of PBF-LB-related volumetric defects [8]. Besides, HPHT™ and HPHT™ + Aged produce nearly identical S–N slopes and similar magnitudes of σ_a, both substantially lower than the as-built fit. These observations indicate that the dominant factors controlling VHCF performance in this alloy are not simply the presence or absence of interior pores, but the net balance between microstructural strengthening and defect severity.

The removal of internal defects by HPHT™ would be expected to increase fatigue life because pores are efficient crack-initiation sites. However, HPHT™ also fundamentally alters the rapid-solidification microstructure that provides the as-built alloy with high static strength. The as-built PBF-LB microstructure, characterized by a fine cellular network, nanoscale Si precipitates at cell boundaries, and a high degree of supersaturation, yields elevated yield stress. These attributes increase the stress required to nucleate and grow microcracks from small flaws, whether those flaws are pores or persistent slip bands. By contrast, HPHT™ causes grain growth (coarsening), spheroidization of the eutectic Si, loss of supersaturated solute, and relaxation of residual stresses; together, these changes reduce the intrinsic resistance of the matrix to damage accumulation under cyclic loading. The Basquin pre-exponential factors (≈480 MPa for as-built vs. ≈230 MPa for HPHT™ variants) quantify this reduction in the material's fatigue "capacity" beyond defect effects.

The as-built microstructure, despite containing volumetric defects, provides a higher intrinsic stress threshold for microcrack nucleation

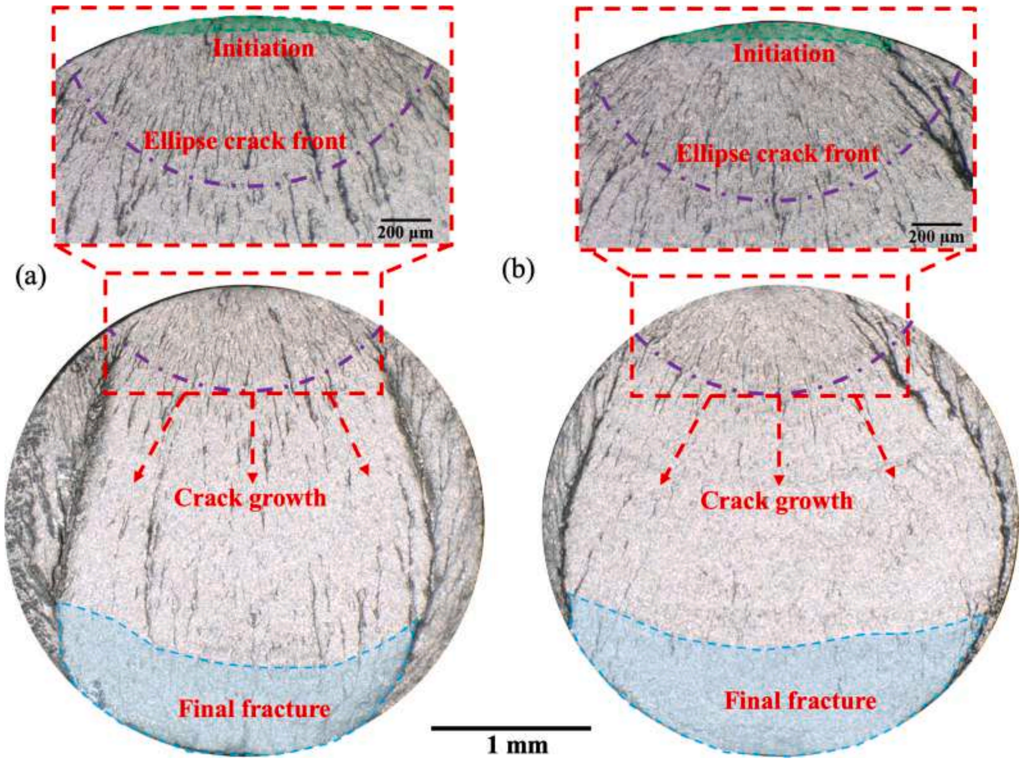

Fig. 19. Optical microscope images of PBF-LB AlSi7Mg alloy fracture surfaces, highlighting surface crack initiation, propagation, and final fracture, (a) Specimen S3 (HPHT™ only, 80 MPa, 2.15×10^8 cycles) and (b) Specimen S15 (HPHT™ + Aged, 80 MPa, 8.18×10^8 cycles).

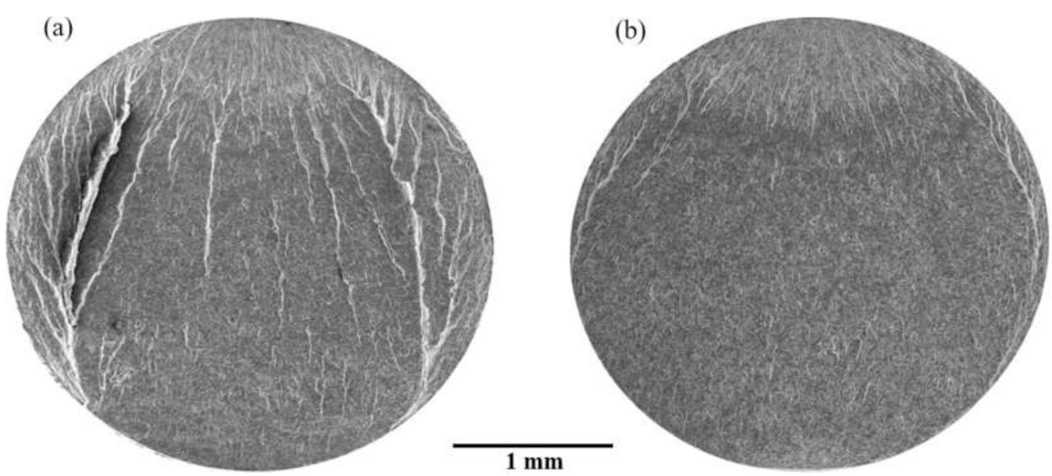

Fig. 20. SEM images of the fracture surfaces of specimens subjected to the same stress amplitude of 85 MPa; (a) specimen S5 (HPHT™, 3.51×10^7 cycles), (b) specimen S18 (HPHT™ + Aged, 1.76×10^8 cycles).

because of solid-solution and grain boundary-related strengthening (Hall-Petch effect), and because residual tensile/compressive stress patterns and the fine Si network impede early dislocation accumulation. Thus, the elevated baseline strength of the as-built condition can compensate for the presence of pores and, in aggregate, produce superior VHCF performance compared with "defect-free" HPHT™ material whose matrix is softer and more permissive to cyclic slip.

This interpretation is consistent with the similar slopes of the HPHT™ and HPHT™ + Aged fits: aging restores some strength via precipitation hardening (β″), raising σ_a slightly relative to HPHT™ −only, but it does not restore the unique rapid-solidification architecture; consequently, the HPHT™ + Aged condition remains well below the as-built Basquin curve. Practically, these results emphasize that HPHT™ alone may not contribute to enhanced VHCF performance. Improvements in VHCF performance should therefore target both defect elimination and retention or recovery of matrix strengthening (for example, through optimized HIP thermal cycles that limit coarsening, controlled quench + aging schedules to maximize precipitation strengthening, or complementary surface treatments such as shot peening or laser re-melting to raise near-surface resistance to initiation).

3.5. Post-mortem fractography

Optical Microscopy (OM) and SEM based post-mortem fractography analyses were conducted on the failed specimens to better comprehend the factors that were responsible for the crack initiation and final failure in the PBF-LB AlSi7Mg specimens. In all conditions, the fatigue crack started from the surface rather than by internal defect-driven crack

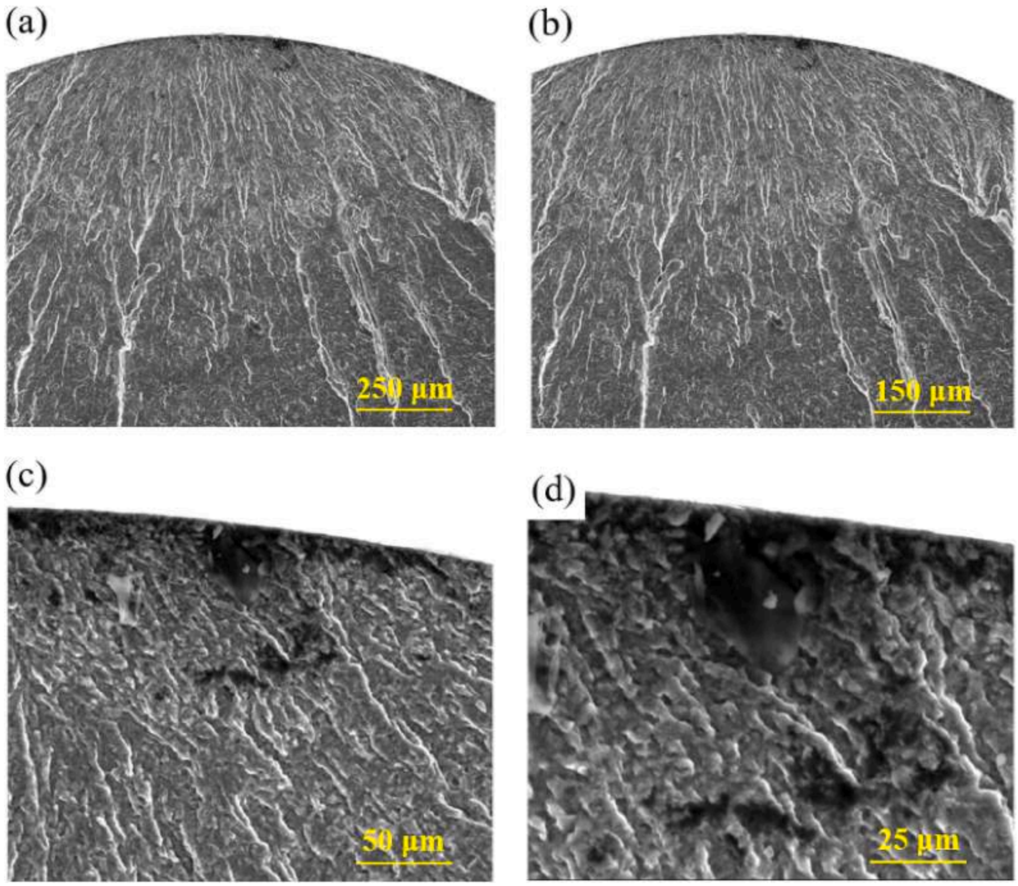

Fig. 21. SEM fractography of the fracture surface of specimen S5 (HPHT^{TM}, 3.51 $\times$ 10^7 cycles) subjected to a stress amplitude of 85 MPa, showing crack initiation from the surface in different magnifications.

initiation. For instance, Fig. 19 shows OM fractographic analysis of Specimen S3 (HPHT^{TM} only, 80 MPa, 2.15 $\times$ 10^8 cycles) and Specimen S15 (HPHT^{TM} + Aged, 80 MPa, 8.18 $\times$ 10^8 cycles). The shaded green area shows the surface-mediated crack initiation area. The advancing crack front displayed an elliptical arc profile, with the center of this ellipse located at the surface site where the crack first initiated.

The HPHT^{TM}-only fracture surface (Fig. 19a) shows a coarser, slightly rougher appearance with distinct radial features and a few pronounced ribs/steps near the perimeter. Distinct radial markings originate from a surface-initiating site, indicating early crack nucleation followed by rapid propagation under cyclic loading. Although HPHT^{TM} effectively reduced the population of internal pores formed during laser powder bed fusion, it does not modify the surface condition or remove near-surface stress concentrators such as partially melted particles, adhered spatters, or machining-induced microdefects. The rough and irregular fracture topography suggests that these surface irregularities, combined with localized microstructural heterogeneity near melt pool boundaries, facilitated crack initiation.

The specimen subjected to HPHT^{TM} followed by artificial aging (Fig. 19b) exhibited a noticeably different fracture morphology, despite sharing the same surface-origin initiation mechanism. The overall fracture surface was smoother and more uniform, with finer radial markings and fewer secondary cracking features. The low-temperature aging treatment promoted the formation of a dense dispersion of nanoscale Mg_2Si precipitates within the aluminum matrix, enhancing the yield stress and microstructural stability without causing severe coarsening of the silicon phase. This precipitate strengthening reduced cyclic slip localization near the surface and delayed crack initiation even in the presence of minor surface asperities. The combination of pore closure by HPHT^{TM} and precipitation hardening through aging led to slower crack growth kinetics and a more stable propagation path.

The comparison of these two conditions highlights that surface integrity and microstructural stability, rather than internal porosity, controlled the VHCF of PBF-LB AlSi7Mg in the VHCF regime. While HPHT^{TM} effectively addressed volumetric defects, it did not mitigate the role of surface defects as primary initiation sites. The subsequent aging treatment refined the precipitation state of the matrix and reduced strain localization. These results highlight that optimizing both subsurface defect morphology and the near-surface microstructure through tailored post-processing is essential to achieve extended fatigue life under long-term cyclic loading conditions.

Fig. 20 compares the SEM-based fracture morphology of specimens S5 (HPHT^{TM}, 3.51 $\times$ 10^7 cycles) and S18 (HPHT^{TM} + Aged, 1.76 $\times$ 10^8 cycles) subjected to the same stress amplitude of 85 MPa. The aged specimen (S18) exhibited an approximately fivefold increase in fatigue life compared with the HPHT^{TM} −only specimen (S5). In both cases, cracks initiated from the surface; however, the fracture surface of S18 was noticeably smoother than that of S5. Fig. 21 shows SEM fractographs of specimen S5 (HPHT^{TM} condition, 3.51 $\times$ 10^7 cycles at a stress amplitude of 85 MPa) captured at progressively higher magnifications to elucidate the crack-initiation and early crack-growth features. At higher magnification, the near-surface region (adjacent to the specimen surface) exhibits tortuous markings and localized surface irregularities, indicating the crack-initiation site.

Figs. 22 and 23 compare detailed fracture morphology (at various magnifications) of specimens S2 (HPHT^{TM}, 5.46 $\times$ 10^8 cycles) and S14 (HPHT^{TM} + Aged, 8.12 $\times$ 10^8 cycles) subjected to the same stress amplitude of 77.5 MPa. These two specimens showed the longest fatigue life corresponding to their heat treatment condition. Both fracture surfaces indicate a surface-origin fatigue crack initiation, followed by stable

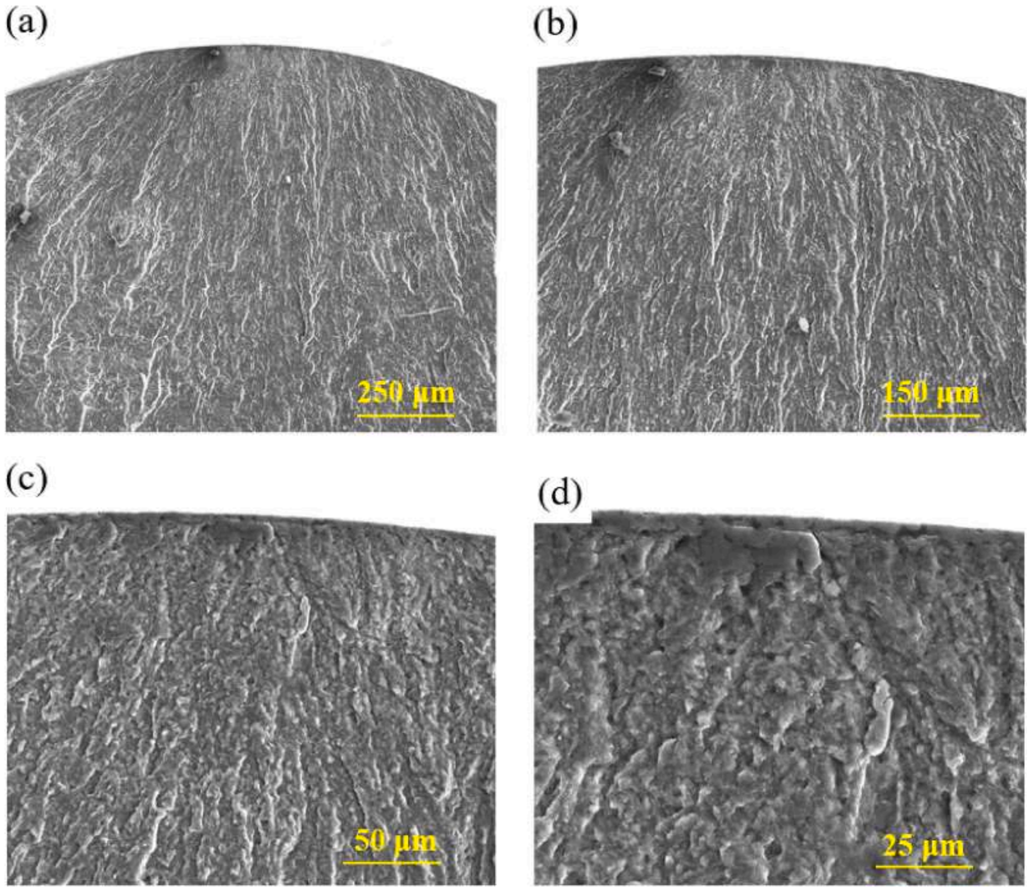

Fig. 22. SEM fractography of the fracture surface of specimen S2 (HPHT^{TM}, 5.46×10^8 cycles) subjected to a stress amplitude of 77.5 MPa, showing crack initiation from the surface in different magnifications.

crack propagation into the bulk. At low magnification (a–b), the crack-initiation site is located at/near the specimen free surface, and the surrounding fracture morphology reveals a radially spreading fatigue region with directional crack-growth markings extending away from the surface. Even when internal volumetric defects are mitigated through HPHT^{TM}, surface-related stress concentrators (e.g., minor surface imperfections or near-surface heterogeneities) remain largely unaffected by densification. In the VHCF regime, where applied stress amplitudes are low, and crack initiation governs most of the fatigue life, such surface features become particularly critical. Accordingly, in the absence of dominant interior defects after HPHT^{TM}, the controlling crack-initiation mechanism shifts toward the surface or near-surface region. No interior "fisheye"–type initiation is evident. At higher magnification (c–d), the near-surface initiation zone becomes clearer and is characterized by tortuous fatigue markings, localized surface irregularities, and a rougher micro-tearing morphology, consistent with crack nucleation from a surface stress concentrator (e.g., minor surface imperfection or microstructural heterogeneity) and subsequent short-crack growth.

4. Conclusions

Based on the combined SEM/EBSD/TEM characterization, XCT porosity analysis, tensile behavior, ultrasonic fatigue testing (20 kHz, $R = -1$), and post-mortem fractography, the following conclusions are drawn:

- The rapid-solidification substructure is dissolved during HPHT^{TM}, leading to a coarse α-Al matrix with spheroidized/coarsened Si particles and reduced microstructural heterogeneity.
- For the HPHT^{TM} + age condition, fine β″/GP-zone precipitates form after aging and increase matrix strength relative to HPHT^{TM} –only, but the loss of the as-built cellular network and supersaturation-driven strengthening is irreversible.
- Equivalent pore sizes remained ~ 10–20 µm in both conditions (HPHT^{TM} and HPHT^{TM} + aged), with only a slight reduction in average defect size after aging, indicating negligible influence of aging on volumetric defects.
- The fatigue strength at 10^9 cycles drops from ~ 479.8 MPa (as-built) to ~ 225–231 MPa (HPHT^{TM} and HPHT^{TM} + aged), showing that microstructural softening dominates long-life fatigue resistance despite defect mitigation.
- Fractography consistently showed surface/near-surface initiation, indicating that near-surface stress concentrators govern VHCF life even when internal porosity is largely suppressed.

In summary, this study demonstrated that HPHT^{TM} effectively densifies and homogenizes PBF-LB AlSi7Mg, while subsequent aging introduces precipitation strengthening; however, the accompanying loss of as-built microstructural strengthening leads to markedly reduced VHCF performance. These results highlight the competing roles of defect mitigation and matrix softening, and they provide practical guidance for optimizing post-processing routes for gigacycle fatigue reliability in additively manufactured Al–Si–Mg alloys.

Data availability

Data will be made available on request.

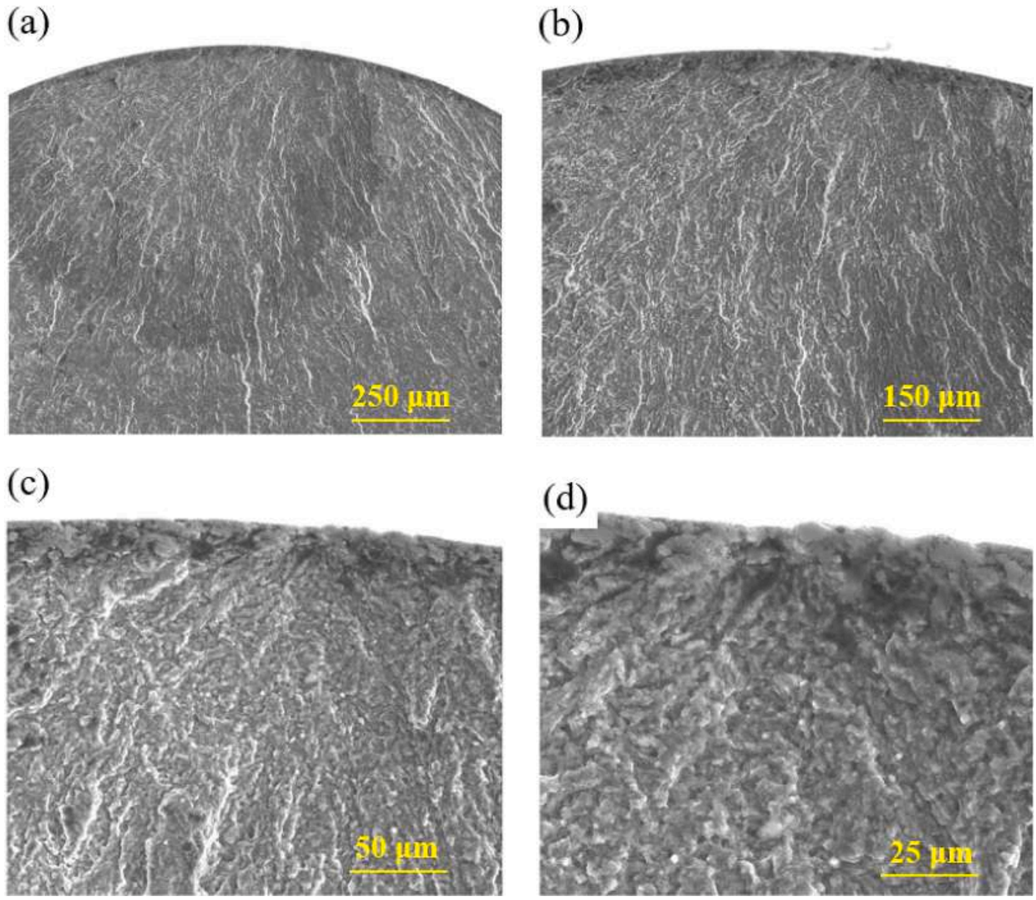

Fig. 23. SEM fractography of the fracture surface of specimen S14 (HPHT^{TM} + Aged, 8.12×10^8 cycles) subjected to a stress amplitude of 77.5 MPa, showing crack initiation from the surface in different magnifications.

CRediT authorship contribution statement

Dinesh Shivakoti: Writing – original draft, Methodology, Investigation, Formal analysis. **Marta Gajewska:** Writing – original draft, Methodology, Investigation, Formal analysis, Data curation. **Mojtaba Roshan:** Writing – original draft, Methodology, Investigation. **MohammadBagher Mahtabi:** Writing – original draft, Methodology, Investigation. **Grzegorz Cios:** Writing – review & editing, Software, Methodology. **Wiktor Bednarczyk:** Writing – review & editing, Software, Methodology. **Donald Godfrey:** Writing – review & editing, Resources. **Francisco Medina:** Writing – review & editing, Resources. **Chad Beamer:** Writing – review & editing, Resources. **Andrew Cassese:** Writing – review & editing, Resources. **Andrea Tridello:** Writing – review & editing, Software, Methodology. **Alessandro Benelli:** Writing – review & editing, Software, Methodology. **Meysam Haghshenas:** Writing – review & editing, Supervision, Project administration, Funding acquisition, Formal analysis, Conceptualization.

Declaration of competing interest

The authors declare that they have no known competing financial interests or personal relationships that could have appeared to influence the work reported in this paper.

References

[1] M. Tocci, A. Pola, M. Gelfi, G.M. La Vecchia, Effect of a New High-pressure Heat Treatment on Additively Manufactured AlSi10Mg Alloy, Metall. Mater. Trans. A 51 (9) (2020) 4799–4811.
[2] K. Tahmasbi, M. Muhammad, M. Avateffazeli, M. Yaghoobi, A. Tridello, D. S. Paolino, S. Shao, N. Shamsaei, M. Haghshenas, Very high cycle fatigue characteristics of laser beam powder bed fused AlSi10Mg: a systematic evaluation of part geometry, Int. J. Fatigue 189 (2024) 108544.
[3] S.I. Shakil, W. Bednarczyk, M. Gajewska, Z. Mahbooba, A. Saharan, A. Tridello, A. Benelli, M. Haghshenas, Microstructure, mechanical properties, and fatigue performance of a PBF-LB Al2139ZrTi alloy, Int. J. Fatigue 109245 (2025).
[4] S.I. Shakil, A. Hadadzadeh, B.S. Amirkhiz, H. Pirgazi, M. Mohammadi, M. Haghshenas, Additive manufactured versus cast AlSi10Mg alloy: Microstructure and micromechanics, Results in Materials 10 (2021) 100178.
[5] F. Alghamdi, X. Song, A. Hadadzadeh, B. Shalchi-Amirkhiz, M. Mohammadi, M. Haghshenas, Post heat treatment of additive manufactured AlSi10Mg: on silicon morphology, texture and small-scale properties, Mater. Sci. Eng. A 783 (2020) 139296.
[6] V.A. Medrano, E. Arrieta, J. Merino, B. Ruvalcaba, K. Caballero, B. Ramirez, J. Diemann, L.E. Murr, R.B. Wicker, D. Godfrey, M. Benedict, F. Medina, A comprehensive and comparative study of microstructure and mechanical properties for post-process heat treatment of AlSi7Mg alloy components fabricated in different laser powder bed fusion systems, J. Mater. Res. Technol. 24 (2023) 6820–6842.
[7] J. Diaz, K. Caballero, V.A. Medrano, E. Arrieta, M. Benedict, D. Godfrey, R.B. Wicker, F. Medina, Comparison of Multiple Heat Treatments by Observing Mechanical Properties and Microstructure of LPBF Fabricated Aluminum F357, Solid Freeform Fabrication 2022: Proceedings of the 33rd Annual International Solid Freeform Fabrication Symposium, 314-324.
[8] M.M.H. Tusher, A. Ince, Exploring VHCF response in L-PBF AlSi7Mg Alloy: Influence of T6 heat treatment on microstructural characteristics and defect distribution, Int. J. Fatigue 187 (2024) 108471.
[9] J.H. Rao, Y. Zhang, A. Huang, X. Wu, K. Zhang, Improving fatigue performances of selective laser melted Al-7Si-0.6Mg alloy via defects control, Int. J. Fatigue 129 (2019) 105215.
[10] N. Sanaei, A. Fatemi, Defects in additive manufactured metals and their effect on fatigue performance: a state-of-the-art review, Prog. Mater Sci. 117 (2021) 100724.
[11] U. Tradowsky, J. White, R.M. Ward, N. Read, W. Reimers, M.M. Attallah, Selective laser melting of AlSi10Mg: Influence of post-processing on the microstructural and tensile properties development, Mater. Des. 105 (2016) 212–222.
[12] L. Girelli, M. Giovagnoli, M. Tocci, A. Pola, A. Fortini, M. Merlin, G.M. La Vecchia, Evaluation of the impact behaviour of AlSi10Mg alloy produced using laser additive manufacturing, Mater. Sci. Eng. A 748 (2019) 38–51.
[13] J. Fiocchi, A. Tuissi, C.A. Biffi, Heat treatment of aluminium alloys produced by laser powder bed fusion: a review, Mater. Des. 204 (2021) 109651.

[14] V.A. Medrano, K. Caballero, E. Arrieta, M. Benedict, R.B. Wicker, F. Medina, Study of Different Aging Conditions for Analysis of Microstructure and Mechanical Properties of F357 Alloy Fabricated in LPBF Printer, Solid Freeform Fabrication 2022: Proceedings of the 33rd Annual International Solid Freeform Fabrication Symposium, 354–363.
[15] V.A. Medrano Balderas, Study of Different Heat Treatments and Aging Conditions for Observing Microstructures and Mechanical Properties of LPBF Fabricated F357 Alloy, ETD Collection for, University of Texas, El Paso, 2023, p. AAI30522503.
[16] C. Beamer, J. Shipley, A. Magnusson, J. Gardstam, P. Burstrom, A. Wessman, D. Godfrey, Uniform rapid quenching of additively manufactured aluminium alloys–a leap forward in quality and performance, DOI: 10.13140/RG.2.2.24741.06886.
[17] C. Beamer, A. Wessman, D. Godfrey, Use of high-pressure heat treatment (HPHTTM) for L-PBF F357, Mater. Res. Proc. 38 (2023) 55–60. https://mrforum.com/product/9781644902837-9.
[18] M. Hamidi Nasab, S. Romano, D. Gastaldi, S. Beretta, M. Vedani, Combined effect of surface anomalies and volumetric defects on fatigue assessment of AlSi7Mg fabricated via laser powder bed fusion, Addit. Manuf. 34 (2020) 100918.
[19] M. Hamidi Nasab, M. Vedani, R.E. Logé, N. Sohrabi, A.M. Jamili, A. du Plessis, S. Beretta, An investigation on the fatigue behavior of additively manufactured laser shock peened AlSi7Mg alloy surfaces, Mater Charact 200 (2023) 112907.
[20] L.F. Leitao Martins, P.R. Provencher, M. Brochu, M. Brochu, Effect of Platform Temperature and Post-Processing Heat Treatment on the Fatigue Life of Additively Manufactured AlSi7Mg Alloy, Metals (2021).
[21] Y. Liu, Y. Wang, X. Luo, Z. Xu, Y. Zhang, G. Ran, H. Wang, Fatigue crack growth behavior and mechanism of AlSi7Mg alloy prepared by laser powder bed fusion, Int. J. Fatigue 204 (2026) 109355.
[22] Q. Zhao, X. Li, J. Hu, Y. Jiang, K. Yang, Q. Wang, Ultra-high cycle fatigue and ultra-slow crack growth behavior of additively manufactured AlSi7Mg alloy, International Journal of Structural Integrity 15 (2) (2024) 382–407.
[23] M. Roshan, M. Mahtabi, W. Bednarczyk, M. Gajewska, G. Cios, Z. Mahbooba, A. Saharan, M. Haghshenas, Powder bed fused–laser beam (PBF-LB) 70/30 copper-nickel (Cu-30Ni): Hierarchical microstructure and mechanical properties, J. Alloy. Compd. 1039 (2025) 183312.
[24] M. Avateffazeli, M. Haghshenas, Ultrasonic fatigue of laser beam powder bed fused metals: a state-of-the-art review, Eng. Fail. Anal. 134 (2022) 106015.
[25] L. Thijs, K. Kempen, J.-P. Kruth, J. Van Humbeeck, Fine-structured aluminium products with controllable texture by selective laser melting of pre-alloyed AlSi10Mg powder, Acta Mater. 61 (5) (2013) 1809–1819.
[26] N. Rojas-Arias, L.F.K. Unti, D.B. Valim, A.H.G. Gabriel, E.B. Fonseca, E.S.N. Lopes, Microstructural Evolution of PBF-LB AlSi10Mg under Different Heat Treatment Conditions, Mater. Res. 28 (Suppl 1) (2025) e20250146.
[27] S. Shi, X. Lin, L. Wang, Z. Wang, L. Wei, H. Yang, Y. Tang, W. Huang, Investigations of the processing–structure–performance relationships of an additively manufactured AlSi10Mg alloy via directed energy deposition, J. Alloy. Compd. 944 (2023) 169050.
[28] T. Bogdanoff, E. Ghassemali, A.E.W. Jarfors, S. Seifeddine, The Impact of HIP Process and Heat Treatment on the Mechanical Behaviour of an Al–Si–Mg Alloy Component, Int. J. Met. 18 (4) (2024) 2882–2892.
[29] S.S. Dash, D. Chen, A review on processing–microstructure–property relationships of Al-Si alloys: recent advances in deformation behavior, Metals 13 (3) (2023) 609.
[30] A.I. Kostyukov, M.G. Baronskiy, T.V. Larina, V.N. Snytnikov, N.A. Zaitseva, A. A. Pochtar, A.V. Ishchenko, S.V. Cherepanova, V.N. Snytnikov, Laser vaporized CrOx/Al2O3 nanopowders as a catalyst for isobutane dehydrogenation, Mater Charact 169 (2020) 110664.
[31] L. Zhou, A. Mehta, E. Schulz, B. McWilliams, K. Cho, Y. Sohn, Microstructure, precipitates and hardness of selectively laser melted AlSi10Mg alloy before and after heat treatment, Mater Charact 143 (2018) 5–17.
[32] E.A. Elsharkawi, E. Samuel, A.M. Samuel, F.H. Samuel, Effects of Mg, Fe, Be additions and solution heat treatment on the π-AlMgFeSi iron intermetallic phase in Al–7Si–Mg alloys, J. Mater. Sci. 45 (6) (2010) 1528–1539.
[33] X. Dong, S. Amirkhanlou, S. Ji, Formation of strength platform in cast Al–Si–Mg–Cu alloys, Sci. Rep. 9 (1) (2019) 9582.
[34] X. Dong, P. Li, S. Amirkhanlou, S. Ji, P.S. Popel, U. Dahlborg, M. Calvo-Dahlborg, Evidence of disruption of Si-rich microstructure in engineering-lightweight Al–12.2 at.% Si alloy melt above liquidus temperature, Sci. Rep. 10 (1) (2020) 12979.
[35] X. Fang, M. Song, K. Li, Y. Du, Precipitation sequence of an aged Al-Mg-Si alloy, J. Min. Metall. Sect. B. 46 (2) (2010) 171–180.
[36] B. Chen, S.K. Moon, X. Yao, G. Bi, J. Shen, J. Umeda, K. Kondoh, Strength and strain hardening of a selective laser melted AlSi10Mg alloy, Scr. Mater. 141 (2017) 45–49.
[37] P. Ashwath, M.A. Xavior, A. Batako, P. Jeyapandiarajan, J. Joel, Selective Laser Melting of Al–Si–10Mg Alloy: Microstructural Studies and Mechanical Properties Assessment, Journal of Materials Research and Technology 17 (2022) 2249–2258.
[38] G. Di Egidio, L. Tonelli, M. Zanni, D. Carosi, A. Morri, L. Ceschini, Direct artificial aging of the PBF-LB AlSi10Mg alloy designed to enhance the trade-off between strength and residual stress relief, Journal of Alloys and Metallurgical Systems 5 (2024) 100063.
[39] H.R. Kotadia, G. Gibbons, A. Das, P.D. Howes, A review of Laser Powder Bed Fusion Additive Manufacturing of aluminium alloys: Microstructure and properties, Addit. Manuf. 46 (2021) 102155.
[40] P. Snopiński, K. Matus, M. Król, T. Warski, M. Kotoul, M. Barlak, K. Nowakowska-Langier, Thermal stability and Ar+ ion irradiation behaviour of SLM AlSi10Mg alloy post-processed via KOBO extrusion method, J. Therm. Anal. Calorim. 150 (2) (2025) 991–1012.
[41] A. Aydin, E. Cetin, K. Mumtaz, In-situ Dynamic laser area heating during diode point melting for thermal gradient reduction in laser powder bed fusion, Mater. Des. 114985 (2025).
[42] L. Dai, C. Song, H. Fu, H. Chen, Z. Yan, Z. Liu, R. Li, A. Wang, Y. Yang, J.-K. Yu, Recrystallization induced by heat treatment regulates the anisotropic behavior of CoCrMo alloys fabricated by laser powder bed fusion, Materials Futures 4 (2) (2025) 025001.